**Published on Metallurgical & Materials Transactions B, Submitted on July 8, 2003, Revised on Nov. 26, 2003, Accepted on March 1, 2004**

# STUDY OF TRANSIENT FLOW AND PARTICLE TRANSPORT IN CONTINUOUS STEEL CASTER MOLDS: PART I. FLUID FLOW

Quan Yuan, Brian G. Thomas and S. P. Vanka

University of Illinois at Urbana-Champaign,
Department of Mechanical and Industrial Engineering,
1206 West Green Street,
Urbana, IL USA 61801
Ph: 217-244-2859, 217-333-6919; Fax: 217-244-6534
Email: quanyuan@uiuc.edu, bgthomas@uiuc.edu, spvanka@uiuc.edu

## ABSTRACT

Unsteady three-dimensional flow in the mold region of the liquid pool during continuous casting of steel slabs has been computed using realistic geometries starting from the submerged inlet nozzle. Three large-eddy simulations have been validated with measurements and used to compare results between full-pool and symmetric half-pool domains and between a full-scale water model and actual behavior in a thin-slab steel caster. First, time-dependent turbulent flow in the submerged nozzle is computed. The time-dependent velocities exiting the nozzle ports are then used as inlet conditions for the flow in the liquid pool. Complex time-varying flow structures are observed in the simulation results, in spite of the nominally steady casting conditions. Flow in the mold region is seen to switch between a "double roll" recirculation zone and a complex flow pattern with multiple vortices. The computed time-averaged flow pattern agrees well with measurements obtained by hot-wire anemometry and dye injection in full-scale water models. Full-pool simulations show asymmetries between left and right sides of the flow, especially in the lower recirculation zone. These asymmetries, caused by interactions between two halves of the liquid pool, are not present in the half-pool simulation. This work also quantifies differences between flow in the water model and the corresponding steel caster. The top surface liquid profile and fluctuations are predicted in both systems and agree favorably with measurements. The flow field in the water model is predicted to differ from that in the steel caster in having higher upward velocities in the lower mold region and a more uniform top surface liquid profile. A spectral analysis of the computed velocities shows characteristics similar to previous measurements. The flow results presented here are later used (in Part II) to investigate the transport of inclusion particles.

## I. INTRODUCTION

Turbulent flow during the continuous casting of steel is important because it influences critical phenomena that affect steel quality. These include inclusion/bubble transport and entrapment, [1-3] the transport and dissipation of superheat, [4] the shape and fluctuations of the top surface level [5, 6] and the entrainment of mold flux from velocity variations across the top surface. The continuous casting process is schematically shown in Fig. 1, during which the molten steel flows into the liquid pool from the tundish through the submerged entry nozzle (SEN). The flow rate is controlled using either a stopper rod (shown in Fig. 1) or a slide gate that restricts the opening area. The bifurcated or trifurcated nozzle ports direct molten steel jets into the mold cavity at the desired angle with various levels of turbulence and swirl. The water-cooled mold

freezes a thin solid shell, which is continuously withdrawn at the casting speed. The shell contains a large liquid pool, in which steel circulates as shown in Fig. 1.

The flow in both the SEN and the liquid pool is highly turbulent, with Reynolds numbers in excess of 10,000. Thus chaotic turbulent structures exist in the liquid pool even for nominally steady state casting conditions. This might lead to quality problems. The effect of unsteady flow on quality problems has not been investigated, even though many experimental studies have confirmed that transient flow conditions (involving changes in flow patterns) are associated with quality problems. [7] Flow transients influence transport of inclusion particles (e.g. alumina) and bubbles carried by the jets into the liquid pool, and might be the cause for intermittent and asymmetrical defects observed in plants. [7] The turbulent jets traverse the liquid pool and impinge on the narrow face to build up an unsteady heat flux, which might cause shell-thinning breakouts if the instantaneous flux is too high. [8] The top surface, especially near the meniscus, is responsible for surface quality problems and other defects. A liquid slag layer (see Fig. 1) covers the molten steel top surface to prevent it from being re-oxidized by the air. The liquid flux also creeps into the interfacial gap between the mold and the shell to act as a lubricant to prevent surface defects. Excessive fluctuations of the liquid level at the top surface interrupt the steady supply of the liquid slag into the interfacial gap and cause heat transfer variations, resulting in longitudinal cracks, [9] transverse depressions [10] and other defects. [11] The velocity across the top surface also varies with time. Excessive local surface velocity can shear off liquid slag into the liquid pool to form harmful mold slag inclusions, [12] causing skin delaminations, slivers and other defects in rolled sheet product. [7] Heat transfer at the top surface is also important. If the surface temperature is too cold and the flow is too slow, the meniscus might solidify to form hooks or deep oscillation marks. Plant observations have found that these defects are intermittent, [13] suggesting that they are related to flow transients. The present work aims to generate fundamental insights into the transient flow in the mold region, as an essential step towards minimizing defects in the final steel product.

Many previous studies have used Reynolds-averaged turbulence models (mainly the k-ε model) to study flow in the liquid pool. [14-22] These models predict time-averaged velocities with reasonable accuracy [21] and at a reasonable computational cost. However, they poorly estimate turbulent dynamics such as quantified by *rms* (root mean square) values. [21] A transient Reynolds averaged approach, which is more computationally demanding, was used previously to study transient changes in flow pattern resulting from drastic changes in inlet conditions. [23] However this approach was unable to capture inherent flow transients during steady casting in several test cases. This may be due to the large numerical dissipation associated with these models, or due to the assumption of isotropic turbulence.

The present work employs the Large Eddy Simulation (LES) approach. This approach was shown in recent studies to accurately predict the dynamics of large-scale turbulence structures during continuous casting of steel. [21, 22, 24-26] However LES entails many challenges when applied to this complex flow problem, including the prescription of the transient inlet velocities, resolution of the complex domain geometry, the moving solidification front and computing long-term transients. Therefore, the application of LES to these aspects of continuous casting requires large amount of computer memory and CPU time. As a result, this model may be considered as a way to generate fundamental understanding and benchmarks for simple models rather than as an engineering tool for parametric study.

Due to the high operating temperature, it is difficult and expensive to conduct flow measurements in continuous steel casters in order to validate model predictions. [21] However,

because of the nearly equal kinematic viscosities of molten steel and water, water models with transparent plastic walls can be used to study single-phase flow in steel casting processes, [27, 28] [5, 29-32] where Froude similarity is usually employed. Thus, measurements using dye injection, hot-wire anemometry and Particle Image Velocimetry (PIV) to quantify the flow velocities in water models are used to validate the predictions of the LES code in this work.

Although very valuable for validation of computational models, the water model differs from the actual steel caster in several aspects important to the flow field. First, its sidewalls, which represent the moving solidifying shell front, are non-porous and stationary. Further, the water model has a flat bottom with outlet ports instead of the long tapering molten steel pool. These two major differences give rise to different flow phenomena, as this work will show.

Three simulations are presented in this paper to understand the differences between full-pool and symmetric half-pool domains and between full-scale water model and real steel caster behavior. The first simulation (*Case 1*) is on a full-scale water model corresponding to a standard slab caster. A symmetry condition was imposed at the center plane between narrow faces so only half of the physical liquid pool (Fig. 2(a)) is simulated (Fig. 2(b)). The next two cases simulate the full pool of a thin-slab caster water model (*Case 2-W*) and its corresponding steel caster (*Case 2-S*). Detailed information on the computational model and the three simulations are given in the next section. This is followed by results from the three simulations. Comparisons with measurements are made where available, including velocities along the jet and across the top surface, the profile of the top surface liquid level and a spectral analysis. The turbulent flow structures in the pool are presented, along with the transient flow asymmetries. The flow field is quantified with the time-averaged and *rms* velocities along the jets, across the top surface and in the lower recirculation zone. This paper also quantifies the differences between the velocity field in the water model and the corresponding steel caster, including the top surface liquid profile.

## II. MODEL DESCRIPTION

The unsteady three-dimensional Navier-Stokes equations governing the flow field are given by:

$$\frac{\partial \mathrm{v}_i}{\partial x_i} = 0 \qquad [1]$$

$$\frac{D\mathrm{v}_i}{Dt} = -\frac{1}{\rho}\frac{\partial p}{\partial x_i} + \frac{\partial}{\partial x_j}\nu_{eff}\left(\frac{\partial \mathrm{v}_i}{\partial x_j} + \frac{\partial \mathrm{v}_j}{\partial x_i}\right) \qquad [2]$$

where:

$$\nu_{eff} = \nu_0 + \nu_t \qquad [3]$$

$$\nu_t = 0.01(\Delta x \Delta y \Delta z)^{2/3}\sqrt{\frac{\partial \mathrm{v}_i}{\partial x_j}\frac{\partial \mathrm{v}_i}{\partial x_j} + \frac{\partial \mathrm{v}_i}{\partial x_j}\frac{\partial \mathrm{v}_j}{\partial x_i}} \qquad [4]$$

In the context of a large eddy simulation (LES), these velocities represent the large scale eddies with the influence of small scale eddies being represented by sub-grid scale (SGS) models. In the above equations, $\mathrm{v}_i$ is the three-dimensional time-dependent velocity vector representing the motion of large eddies, and $\Delta x$, $\Delta y$ and $\Delta z$ are the size of each cell in the Cartesian computational grid. The eddy viscosity $\nu_t$ can be computed using SGS models to represent the

dissipative effect of the unresolved small eddies. It vanishes if the grid resolution is capable of resolving the smallest eddies (Kolmogorov scale). Equation [4] describes the evolution of the traditional Smagorinsky SGS model, [33] which was used in the first computation as a preliminary exercise. In the other two computations, the eddy viscosity was set to zero. These no-SGS model simulations could be interpreted as coarse grid DNS (direct numerical simulations), as the effect of the SGS model was considered to be small, as discussed elsewhere. [34]

**A. Boundary Conditions**

1. *Inlet*

The liquid pool is fed by a bifurcated (*Case 1*) or trifurcated (*Case 2*) nozzle, which has an important influence on the flow pattern. [21] Thus nozzle simulations were first conducted to acquire accurate inlet conditions. Unsteady flow velocities leaving the nozzle ports were collected every 0.001s. The time-dependent velocities were stored and then recycled periodically as the inlet conditions for the liquid pool simulations. More details of the inlet nozzle simulations are given later.

2. *Outlet*

One of the important differences between water models and steel casters is that water models have outlet ports on their plastic bottom or side walls, while in steel casters the liquid pool gradually tapers to a solid end. In this work, the computational domain of the water model (*Case 1*) is the same as the physical model. However, the domain extent of the thin-slab caster (*Case 2*) is limited by computational resources. For computational efficiency, simulations of *Case 2* only compute flow in the mold liquid pool from the top surface to a depth of 1.2m (water model) or 2.4m (steel caster) below the top surface. This creates an artificial outlet plane where flow leaves the computational domain. In current simulations, a constant pressure boundary condition, with zero gradient of other variables, was used at this plane where the flow becomes nearly uniform.

3. *Top Surface and Symmetry Center Plane*

The symmetry plane condition was only imposed in the half pool simulation, *Case 1.* A free-slip condition was imposed along both the top surface and the center plane. Specifically, along these two boundaries the normal velocity was constrained to zero, and the normal gradients of pressure and the other two velocity components were set to zero. The predictions and measurements of this work (presented later) suggest that the top surface is relatively quiescent, so no model of free surface deformation is necessary to accurately model the flow. The effect of the symmetry plane condition is investigated by comparing full pool and half pool simulations.

4. *Narrow Face and Wide Face Walls*

Water models and steel casters are very different at the narrow and wide face walls. Water models have stationary straight plastic side walls representing the solidification front. Thus all three velocity components were set to zero at the wall boundary. However, flow in the steel caster was modeled up to, but not including, the front of the downward moving mushy zone, [20] where solidification occurs to take away mass from the molten steel pool. This required tapering the domain walls to include only the liquid pool. To further account for the solidification and downward motion, a velocity boundary condition given by Eq. [5] was used:

$$\mathrm{v}_x = V_n \cos\theta - V_t \sin\theta = \left(\frac{\rho_s}{\rho_l} - 1\right)\sin\theta\cos\theta V_{casting} \qquad [5a]$$

$$\mathrm{v}_z = V_n \sin\theta + V_t \cos\theta = \left(\frac{\rho_s}{\rho_l}\sin^2\theta + \cos^2\theta\right)V_{casting} \qquad [5b]$$

Derivation of Eq. [5] can be found in the Appendix. In both systems, no wall functions were used to represent near wall turbulence, because of a relatively fine mesh near the wall.

**B. Solution Procedure**

The time-dependent three-dimensional Navier-Stokes equations are discretized using the Harlow-Welch fractional step procedure. [35] Second order central differencing is used for the convection terms and the Crank-Nicolson scheme [36] is used for the diffusion terms. The Adams-Bashforth scheme [37] is used to discretize in time with second order accuracy. The pressure Poisson equation is solved using either a Fast Fourier Transform (FFT) solver [38] in *Case 1* with a structured grid or an algebraic multi-grid (AMG) solver [39] in *Case 2* with unstructured Cartesian grids.

**C. Computational Details**

The three computational domains are presented in Fig. 2. The geometry, casting conditions, material properties and computational parameters are given in Table I. For computational efficiency, the domain was divided into nozzle and liquid pool regions. Flow in each region was computed separately. Nozzle simulations were first performed, from which transient velocities exiting the nozzle ports were collected and used as conditions at the pool inlet.

1. *Case 1*

Figure 2(a) shows the physical water model of a standard slab caster (*Case 1*). Water enters the liquid pool from the bifurcated nozzle ports at a downward angle of approximately 25 degrees. Water exits the model from four outlet pipes near the bottom of the wide face, as shown in Fig. 2(a). Detailed geometry and operation conditions are published elsewhere. [1, 28]

This half pool simulation adopted velocity profiles from a prior turbulent pipe flow simulation as the inlet velocities from the small, elliptical nozzle ports. The pipe was 38% open at its entry where a constant velocity was imposed. Transient velocities were collected 7.5 pipe diameters away from the pipe entry for 1.6s and then rotated 25˚ downward to feed the pool simulation.

Figure 2(b) shows the half pool computational domain with a symmetry condition at the pool center. The nozzle port was modeled as an opening on the symmetry plane. The outlet ports, which are far from our flow region of interest, were approximated as square openings with the same area as the physical ports. This computational domain was discretized with a structured Cartesian grid consisting of 1.6 million cells. The time step of the simulation was 0.0008s.

2. *Case 2*

Domains of a thin slab steel caster (*Case 2-S*) and its water model (*Case 2-W*) are presented in Figs. 2 (d) and (c) respectively. Both systems used the same 1.1-m long, inlet nozzle, starting from the tundish bottom and fed through the annulus formed by a 64.4% open stopper rod, down a 70-mm diameter round bore upper nozzle that tapered into a thin trifurcated outlet region. A prior nozzle simulation with realistic geometry was performed with a 0.6 million cell

mesh using an unstructured Cartesian cell code. Time-dependent velocities leaving the trifurcated nozzle ports were stored every 0.025s for 9.45s (10-day computation on PentiumIV 1.7GHz CPU) to be used as inflow to the liquid pool.

Figure 2(d) shows that the domain of the steel caster has a curved side boundary, which represents the solidifying front at the liquidus temperature. The boundary shape was obtained from the prediction of an in-house code, CON1D, [40] [41] which is shown to agree with measurements (Fig. 3) on a breakout shell. [42] It should be noted that the symmetry plane assumption was not needed in the two full pool simulations. There is no argon gas in any of the simulations in order to match the real caster, where calcium treatment was used to avoid nozzle clogging.

Unstructured Cartesian grids consisting of 0.7 million and 1.3 million cells were employed for the water model and the steel caster simulations respectively. The latter grid features cells centered 0.25mm from the wall in the upper mold including the impingement region. This half-cell size gradually increases to a maximum of 7.1mm in the lower-gradient interior of the domain. The time step of 0.001s was used in both simulations. The simulation took 29.5 CPU seconds per time step on a Pentium IV 1.7GHz PC for the 1.3 million cells grid or 24 days for 70,000 time steps (70 seconds of real time) with the AMG solver. Compared to the AMG, the FFT solver is about four times faster and takes about one quarter of the memory. However, it is not suitable for complex geometries that are necessary to represent the actual caster.

## III. RESULTS

### A. The Standard Slab Caster Water Model (*Case 1*)

*Case 1* is a half pool simulation to model a typical slab caster with bifurcated nozzles. Its transient inflow velocities, obtained from the prior pipe simulation, are averaged temporally and shown in Fig. 4(a). Higher velocities are revealed in the lower portion. This is consistent with previous measurements and predictions on similar nozzles. [43, 44] The outward and downward velocity components along the port centerline are depicted in Fig. 4(b), with maximum values at approximately one third distance from the port bottom.

A typical instantaneous velocity field in the liquid pool is shown in Fig. 5. Water emerges from the inlet port as a jet, diffuses as it traverses across the liquid pool, impinges on the narrow face and splits into two recirculation zones consisting of complex structures. The predicted flow pattern matches experimental observations. [1, 28] A closer view of the turbulent structures in the upper roll is presented in Figs. 6(a) and (b) for two time instants. The figures show that the upper roll consists of a relatively simple vortex at the first instant, which evolves to a pattern involving more complex multiple vortices at the second instant. The upper roll alternates irregularly between the two extremes in the simulation. It is also found that, only close to the top surface is the velocity direction consistently horizontal. This is important in understanding the accuracy of the indirect measurement of the flow velocity in steel casters using electromagnetic sensors, [24] which requires a consistent flow direction passing the sensors.

Figure 7 compares the results of the simulation with measurements. The time-averaged speed, $(v_x^2 + v_y^2)^{1/2}$, of the fluid was measured using hot-wire anemometers in a previous work. [28] The measurement was made along four vertical lines in the center plane at specified distances from the SEN. The computation agrees reasonably well with the measurements. The biggest discrepancy occurs along the line 460mm from the SEN, where the predicted maximum speed location is approximately 100mm deeper than the measurement in Set 1. This

might be due to uncertainties in the measurements. It should be noted that significant differences exist between the measured time averages taken at different times, likely due to insufficient time for calculating statistics. More validations of our simulations were made on a 0.4-scale water model and are published elsewhere. [21, 24] They show good agreement between prediction and PIV measurements.

### B. The Trifurcated Inlet Nozzle of Thin Slab Caster (*Case 2*)

A realistic nozzle simulation was conducted to generate accurate unsteady inlet velocities for the computations in the thin slab caster. The computed results are presented in Figs. 8-11. Two typical transient flow patterns are plotted in Fig. 8 showing flow exiting the nozzle ports at different instants. Supplementary to the vector length the arrow darkness also represents the velocity magnitude. In Fig. 8(a), a symmetrical flow pattern is observed between the side ports, while it is apparently asymmetrical in Fig. 8(b). The downward angle of the two side jets varies in time from ~30$^o$ to 45$^o$. The two side jets switch between the two extremes. The jet angle is important because it greatly affects the transport of harmful inclusions carried by the jet entering the liquid pool. Jets at a deeper angle tend to transport more inclusions into the lower roll, encouraging the formation of internal defects such as slivers and blisters (discussed in more detail in Part II). The jet angle is also important as it influences the velocity and the profile of the top surface liquid level. Jets at smaller downward angles are likely to increase the velocity and the liquid level fluctuations along the top surface, by carrying more fluid and momentum into the upper roll. This can cause quality problems as discussed in the previous sections. Accurate prediction of this angle is essential for optimizing the nozzle design. The center jet velocity is seen to fluctuate considerably but the flow pattern in the mold stays nearly the same.

Figure 9 shows the fluctuation of the downward velocity component ($v_z$) sampled at two points, which are symmetrically located on the side port outlet plane with a distance 40mm below the upper edge. Both signals show a mean value of ~0.6m/s but with significant fluctuations. The highest frequency of the signals is around 10Hz. The velocity component is mostly positive, indicating that the flow is mostly downward with occasional upward excursions. Short-term velocity differences are observed between the two sides. However, averaging over a short time is seen to result in approximately the same flow field (see Figs. 10 and 11).

The computed transient velocity fields in the nozzle were averaged over 9.45s (37800 time instants) and plotted in Fig. 10. The velocities of the side jets are quantitatively shown in Fig. 11 along the nozzle port center line. The mean of the side jets is very symmetrical even for a short time (9.45s) of average. Most of the fluid exits the ports from the port center region (20mm-80mm below the upper edge), with some small back flow near the upper and lower edges, where the fluid re-enters the nozzle.

### C. The Thin Slab Water Model (*Case 2-W*)

The transient velocities obtained from the trifurcated nozzle simulation were then used as inflow into the thin slab water model computation. Before showing the computational results, Fig. 12 first presents snap-shots of the dye injection experiment on the water model at four instants, showing the evolution of the transient flow in the liquid pool. Figure 12(a) is at 0.5s after the dye exits the nozzle ports, showing instantaneous jet angles of ~42$^o$ (left) and ~35$^o$ (right). The dye flows with the jet and impinges the narrow face 0.7s later as shown in Fig. 12(b). It then splits into two parts with the flow to move into the lower and upper recirculation zones, as can be seen in plots (c) and (d). The shape of the jets and the lower and upper recirculation zones can be reconstructed from this sequence of four plots. Vortex shedding of

the center jet can also be observed, although it is obscured by the external frame of the water model.

Figures 13 and 14 show a typical instantaneous velocity field and the mean field at the center plane. The mean was obtained over a time of 48.5s. For clarity of presentation, the time-averaged vector plots in this work only show arrows at every second grid point in each direction. The classical double roll flow pattern can be seen in both plots. The shape of the jets and the upper and lower recirculation zones agrees with the dye-injection observation. In contrast to the smooth time-averaged plot, the instantaneous vector plot shows local turbulent structures similar to what was seen in *Case 1*. The oscillation of the center jet observed in the dye injection is also seen in the simulation.

Figure 15 compares the computed time-averaged speed $(v_x^2 + v_z^2)^{1/2}$ with the estimated value from the dye injections along the jet centerline. The solid line denotes the predicted value of the speed averaged over 48.5s. The error bar shows the upper and lower bounds of the transient speed during the 48.5s simulation, indicating a large fluctuation. The dark dots are the estimated transient flow speed obtained by measuring the development of the dye front on the video images. The predicted values reasonably agree with the measurements.

### D. Numerical Model Validation (*Case 2-W*)

Sections III-A and III-C provide model validation with experimental measurements, comparing the predicted and measured velocities along 4 vertical lines (Fig. 7) and along the jet (Fig. 15). Further quantitative experimental validation is provided in sections III-F and H for the top surface velocity and shape respectively. Computational models also require numerical validation to ensure that the effects of grid resolution, time-step size, turbulence model, and discretization errors associated with the order of the numerical scheme are small. Further related issues are the inlet conditions, and symmetry assumption (including half or full mold). This is a complex subject beyond the scope of this paper and is discussed in detail elsewhere. [34, 45] An example is provided here in Fig. 16, which compares the computed speed $(v_x^2 + v_z^2)^{1/2}$ along a vertical line in the caster center plane, midway between the SEN and the narrow face. This figure compares results from three different computational grids: a 0.4 million-node coarse grid, the current 0.7-million node grid, and a 1.4-million-node fine grid. The fine grid included only one half of the domain, so its node spacings are roughly four and eight times finer than the other two grids respectively. The differences between the right and left sides of the domain are more significant than the differences between grids. This indicates that the mesh resolution is adequate. This figure also shows that the effect of adding an SGS k model [46] is very small. This indicates that either the unresolved small turbulent eddies are not very important, or that false diffusion from numerical discretization errors dominates over the sub-grid scale effects.

### E. The Thin Slab Steel Caster (*Case 2-S*)

The steel caster differs from the water model mainly in the solidifying shell boundary and the outlet. In addition, the kinematic viscosity of the molten steel is ~20% smaller than that of water. These differences might lead to a different flow field in a real steel caster, even under the same operating conditions as in the water model. To investigate the flow in the real steel caster, a transient simulation of the thin slab caster was performed using the same unsteady inlet velocities as the water model (*Case 2-W*). The computed instantaneous and time-averaged velocity fields are presented in Figs. 17 and 18 and are qualitatively similar to those of the water model. Both the time averages of the two systems were taken over ~50s. It should be noted that in both cases, the time-averaged center jet is slightly slanted to the left, indicating a long-

term asymmetry. Asymmetries such as these may likely be the cause for the asymmetrical defects observed in steel products.

Figure 19 quantifies the development of the center jet. Both the time-averaged streamwise velocity ($v_z$) and the *rms* values of all three velocity components ($v_x$, $v_y$ and $v_z$) along the jet centerline are shown in the figure. The results reveal that the jet velocity decreases dramatically starting from the nozzle port. The center jet can only penetrate to around 800mm below the center nozzle port. This is important to understanding inclusion transport in the liquid pool. The results also show that the *rms* of the downward velocity is dominant along the center jet, suggesting a strong anisotropy of this turbulent flow.

In Fig. 20, the downward velocity and *rms* values are presented along a line 8.5 center port diameters below the port in the center plane (y=0). The downward velocity at the jet center is seen to decrease to ~45% of the port outlet value. The high velocity near the narrow face front is caused by the side jets. Because of the influence of side jets as well as being confined by the shell, the jet width is smaller than the self-similar free jet. [47] The *rms* distribution again supports the anisotropy of flow in the liquid pool.

### F. Comparison of the Thin Slab Steel Caster and Its Water Model (*Case 2-S* vs. *2-W*)

Flows in the thin slab caster and the water model have been investigated separately. The two systems will be compared here. All the mean values presented in this section were averaged over ~50s. Figure 21 presents the mean of horizontal velocity towards the SEN along the centerline on the top surface. The velocity estimated from the dye injection is also plotted as solid squares in Fig. 21. All the data show a maximum velocity in the middle between the SEN and the narrow face, with a value of ~0.15m/s to ~0.26m/s. A significant asymmetry between the left and right sides is found in the water model (*Case 2-W*), compared to the steel caster (*Case 2-S*). This indicates the existence of a low frequency (lower than 0.02Hz) oscillation between the two sides on the top surface in the water model, which is absent in the simulation of *Case 2-S*. The downward velocity of the shell in the steel caster simulation may have stabilized the flow so that it has less oscillation. Our previous studies of a 0.4-scale water model [24, 48] found a similar oscillation on the top surface with a frequency lower than 0.02Hz. The reason of the oscillation is still not clear. It should be also noted that the velocity on the left side of the water model is very close to that of the steel caster. The *rms* values of the velocities in Fig. 21 are presented in Fig. 22. All the data suggest that the *rms* values reach their maximum at 15mm-30mm away from the SEN and then monotonically decrease towards the narrow face. The predicted *rms* values are large, usually exceeding 30% of the local mean velocities.

Figures 23 and 24 compare the mean and *rms* values of the downward velocity in both systems. The data are extracted along a horizontal line 1000mm below the top surface and 164mm from the narrow face. Figure 23 shows a bigger spatial variation of the downward velocity for the water model. It shows that the steel caster has slower downward flow near the walls (where the shell is found) and less upward (or reverse) flow in the central region. This is likely due to the combined effects of tapering, which restricts the flow domain, the mass loss from solidification, which tends to even the velocity distribution, and the downward withdrawal of the shell, which pulls the flow downwards at the casting speed. An asymmetry between the two sides can be seen for both the water model and the steel caster, again indicating that low frequency oscillations exist with a period longer than 51s.

### G. Velocity Fluctuation on Top Surface

The top surface velocity greatly influences the harmful entrainment of liquid slag. It fluctuates with time due to its turbulent nature. Instantaneous high values of this velocity can shear off fingers of liquid slag into the steel pool [49] to form non-metallic inclusions that cause serious defects. The history of surface velocity variations is investigated in Fig. 25(a), where the time signal of the computed horizontal velocity at the top surface center point (midway between the SEN and the narrow face) for the thin slab steel caster (*Case 2-S*) is plotted. The velocity from the narrow face to the SEN is defined with a positive value in this plot. The figure shows that the amplitude of the fluctuation is comparable to the mean value (Fig. 21). We observed that the velocity occasionally has a sudden "jump" with considerable amplitude (e.g. the flow velocity drops from ~0.4m/s towards the SEN to the opposite direction in 0.2s). Due to a lack of long-term measurements in this caster or the corresponding water model (*Case 2-W*), this behavior is compared with our previous PIV measurements on a 0.4-scale water model shown in Fig. 25(b) and published elsewhere. [50] The figure also shows LES predictions, which were obtained from two half pool simulations (LES1 and LES2) on the 0.4-scale water model. [50] It is observed that the characteristic of large sudden "jumps" was also seen in the PIV measurements but do not exist in the half pool simulations. This suggests that transient interaction between the two halves of the caster likely causes the large sudden jumps. Half pool simulations suppress these sudden jumps by imposing the symmetry boundary condition. The half pool simulations may be missing other such transient phenomena, necessitating full pool simulations.

### H. Liquid Level across Top Surface

Liquid level across the top surface is important because it affects ability of the liquid flux to fill the interfacial gap between the mold and shell, which is important for heat transfer and thereby for surface quality of the final product. Figure 26 shows typical transient top surface levels obtained from the simulation surface pressure results for the thin slab caster and water model. The top surface liquid displacement, $\Delta z$, was estimated from a simple potential energy balance:

$$\Delta z(x,y) = \frac{p(x,y) - p_{mean}}{\left(\rho_l - \rho_{top}\right) g} \qquad [6]$$

Figure 26(a) shows the water model prediction compared with top surface liquid profiles measured from video images at three instants. The predicted surface shape is in reasonable agreement with the measurements. It is also consistent with previous water model results. [51] Figure 26(b) presents the predicted molten steel level at the top surface. The level is always higher near the narrow face, by 2mm in the water model and 4-6 mm in the steel caster. This is because the upward momentum of the liquid near the narrow face lifts the liquid level there. The level change is greater in the steel system because interface movement only requires the displacement of some molten slag. The prediction of the steel caster top liquid profile (Fig. 26(b)) compares reasonably with industry measurements (Fig. 26(b)). [52] Each of nine measurements was obtained by dipping a thin steel sheet into the operating steel caster mold and recording the slag-steel interface shape after removing it. [52] Each point represents the mean deviation of the measurements at that location from the average surface level along the centerline. This average level was determined to be -1.3mm using Eq. [6]. The error bars indicate the range of the measurements at each location. Significant uncertainty in the measurement exists regarding possible rotation of the sheets. The slag layer needs to be thick

enough to cover the steel, in order to provide a steady supply of molten flux into the interfacial gap to lubricate the steel, maintain uniform temperature profiles, and to avoid surface defects in the solid steel product. Thus, the height of this "standing wave" is important to steel quality.

## I. Asymmetries

In most Reynolds-averaged simulations, symmetry is assumed between the flow in the two halves of the liquid pool. This assumption has been shown valid for long-term averages. However, transient flow in the two halves is different, for instance, on the top surface (Figs. 21 and 22) and in the lower roll (Figs. 23 and 24). Figure 27 further reveals the significant flow asymmetry in the lower roll. The signals present the variation of the downward velocity at two pairs of monitoring points, each symmetrically located in the thin slab steel caster. The data were sampled every 0.001s from the simulation results. Shown as solid triangles, the first pair of points is located within the side jets, midway between the SEN and narrow face, 0.3m below the top surface. The other pair is located at 1.2m below the top surface and near (3.5mm to) the narrow faces to illustrate the flow in the lower recirculation zone. The plot on the top shows the velocity history at the first pair of points, which shows similar variations to those in Fig. 9. No long-term asymmetries are observed between these two points in the jets. However, the plot below clearly shows that significant asymmetries can last for a relatively long time (e.g. from 37s to 40s). These observations suggest that (1) low frequency long-term asymmetries exist in the lower recirculation; (2) the asymmetries are due to the turbulent nature of the flow in the liquid pool and not from asymmetries imposed by the inlet jet. This finding is important to the understanding of the behavior of inclusion particles, as particles transported to a deeper location are likely to become permanently entrapped in the steel (as discussed in detail in Part II).

## J. Spectral Analysis

The power spectrum [38] of the turbulent velocity component $v_x$ was calculated at two points in the steel caster, which are symmetrically located in the pool with a distance of 156mm from the SEN outlet, 100mm below the top surface. The spectral analysis was made from 137s of simulation data sampled every 0.001s using the equation below :[38]

$$P(f_k) = \begin{cases} \dfrac{1}{N^2}\left|C_k\right|^2, & k = 0, \dfrac{N}{2} \\ \dfrac{1}{N^2}\left(\left|C_k\right|^2 + \left|C_{N-k}\right|^2\right), & k = 1, \ldots, \dfrac{N}{2} - 1 \end{cases} \qquad [7a]$$

where:

$$C_k = \sum_{n=0}^{N-1} \mathrm{v_x}\left(t_n\right) e^{\mathbf{i}2\pi f_k t_n} \qquad [7b]$$

$$f_k = \frac{k}{t_{N-1} - t_0}, \quad k = -\frac{N}{2}, \ldots, \frac{N}{2} - 1 \qquad [7c]$$

The result in Fig. 28 shows an irregular distribution of the power spectrum, which has high maxima at low frequencies, (less than 1 Hz) and tends to decrease exponentially at higher frequencies, as indicated with the log scale plot. Slight differences exist between the two points, likely due to insufficient sampling time. A similar behavior of the power spectrum was seen in measurements on a scaled water model by Lawson and Davidson. [53]

## IV. CONCLUSIONS

Three-dimensional unsteady turbulent flow in the mold region of the liquid pool of standard and thin slab casters was computed using an in-house Large Eddy Simulation code. The computed velocity fields are compared with measurements and seen to have reasonable agreement. The following observations are concluded from this work:

(1) Complex turbulent structures are observed in the liquid pool. Two typical transient flow structures, consisting of simpler or complex multiple vortices, are found in the upper roll. The vortices break into smaller ones or emerge into bigger ones such that the flow switches between the two patterns.

(2) Flow asymmetries are found in full pool simulations, which includes the short-term asymmetry (e.g. at the nozzle port and along the jet) and the long-term intermittent asymmetry (e.g. on the top surface and in the lower roll). The long-term asymmetry in the lower roll is due to the turbulent nature instead of asymmetries in the inflow.

(3) The interaction between the two halves of the liquid pool causes important transient flow behavior (e.g. sudden jumps of top surface velocity). Imposing an asymmetry assumption suppresses sharp sudden jumps in surface velocities and low frequency flow transients in the lower recirculation zones.

(4) Water models are generally representative of steel casters, especially in the upper region far above the water model outlet. However, steel casters are likely to have somewhat more evenly distributed downward flow in the lower roll zone, where the influence of shell thickness becomes significant.

(5) The top surface level can be reasonably predicted from the top surface pressure distribution. The top surface level profile rises more near the narrow face in the steel caster than in the water model, which has no slag layer to displace.

(6) Our analysis shows anisotropy of turbulent flow in the liquid pool. Spectral analysis suggests that most of the energy is contained in the low frequency region (0-5Hz).

The flow transients and asymmetries have important effects on many other phenomena in the liquid pool that are critical to steel quality. The behavior of inclusion particles will be investigated in the second part of this paper.

## ACKNOWLEDGEMENTS

The authors thank the National Science Foundation (Grant DMI-01-15486) which made this research possible. The work is also supported by the member companies of the Continuous Casting Consortium at University of Illinois at Urbana-Champaign (UIUC). Special thanks are due to Ya Meng for calculating the shell thickness, to Ron O'Malley for plant data and insights into the fluid flow, and the National Center for Supercomputing Applications (NCSA) at UIUC for computational facilities.

## APPENDIX

The effect of the moving solidifying shell on the internal flow in the liquid pool can be represented using a velocity boundary condition, which is illustrated as follows. A stationary control volume in the Euler frame, shown in Fig. A-1, comprises a piece of solid shell. A

normal velocity of the molten steel entering the control volume through the solidification front (sloped edge) can be obtained from mass conservation:

$$\frac{d(\rho_s \mathbf{V})}{dt} = \rho_s A_1 \mathrm{V}_{\mathrm{casting}} + \rho_l A_3 \mathrm{v}_{\mathrm{n}} - \rho_s A_2 \mathrm{V}_{\mathrm{casting}} \qquad \text{[A-1]}$$

By assuming that both the shell shape and the solid density stay constant in this Eulerian frame, the normal velocity can be expressed as:

$$\mathrm{v}_n = \frac{\rho_s (A_2 - A_1)}{\rho_l A_3} V_{casting} = \left( \frac{\rho_s}{\rho_l} \sin\theta \right) V_{casting} \qquad \text{[A-2]}$$

This imposed normal velocity accounts for the mass flow caused by continuous solidification and shell withdrawal. The non-slip condition is assumed to hold tangential to the front:

$$\mathrm{v}_t = V_{casting} \cos\theta \qquad \text{[A-3]}$$

Written in terms of the x, z velocity components:

$$\mathrm{v}_x = \mathrm{v}_n \cos\theta - \mathrm{v}_t \sin\theta = \left( \frac{\rho_s}{\rho_l} - 1 \right) \sin\theta \cos\theta V_{casting} \qquad \text{[A-4a]}$$

$$\mathrm{v}_z = \mathrm{v}_n \sin\theta + \mathrm{v}_t \cos\theta = \left( \frac{\rho_s}{\rho_l} \sin^2\theta + \cos^2\theta \right) V_{casting} \qquad \text{[A-4b]}$$

Eq. [A-4] gives the velocity boundary condition at the shell front position. The value of θ is evaluated at each distance, z, from the slope of the shell thickness profile, given by CON1D in Fig. 3. No adjustment is needed for inside and outside radius because the top 3m of the caster is straight.

## NOMENCLATURE

| | | | |
|---|---|---|---|
| $\frac{D}{Dt}$ | total derivative ($=\frac{\partial}{\partial t} + \mathrm{v}_j \frac{\partial}{\partial x_j}$) | $f_k$ | frequency defined in Eq. [7c] |
| $\mathrm{x}_i$ | coordinate direction (x, y or z) | $\mathbf{i}$ | $\sqrt{-1}$ |
| $\mathrm{v}_i$ | velocity component | $A$ | area |
| $\nu_0$ | kinematic viscosity of fluid | $V_{\mathrm{casting}}$ | casting speed |
| $\nu_{eff}$ | effective viscosity of turbulent fluid | $N$ | total sampling time steps in Eq.[7] |

| | |
|---|---|
| $\rho$ | density |
| $p$ | static pressure |
| $p_{mean}$ | average pressure over top surface |
| $t$ | time |
| $g$ | gravity acceleration ($9.81 m^2/s$) |
| $P$ | power spectrum defined in Eq. [7a] |
| $\lvert C_k \rvert$ | modulus of $C_k$ in Eq. [7b] |

Subscripts:

| | |
|---|---|
| $l$ | fluid (liquid steel or water) |
| $s$ | solid |
| $top$ | top surface material (air or slag) |
| $n, t$ | normal, tangential |
| $i, j$ | direction (x, y, z) |
| | repeated indices imply summation |

## REFERENCE


1. R.C. Sussman, M. Burns, X. Huang and B.G. Thomas: "Inclusion Particle Behavior in a Continuous Slab Casting Mold", in *10th Process Technology Conference Proc.*, vol. 10, Iron and Steel Society, Warrendale, PA, 1992, pp. 291-304.
2. Y. Ho, C. Chen and W. Hwang: "Analysis of Molten Steel Flow in Slab Continuous Caster Mold", *ISIJ International,* 1994, vol. 34 (3), pp. 255-64.
3. B. Grimm, P. Andrzejewski, K. Muller and K.-H. Tacke: "Inclusions in Continuously Cast Steel Slabs-Numerical Model and Validation", *Steel Res.,* 1999, vol. 70 (10).
4. X. Huang, B.G. Thomas and F.M. Najjar: "Modeling Superheat Removal during Continuous Casting of Steel Slabs", *Metall. Trans. B,* 1992, vol. 23B (6), pp. 339-56.
5. D. Gupta and A.K. Lahiri: "Water-Modeling Study of the Surface Disturbances in Continuous Slab Caster", *Metallurgical and Materials Transactions B,* 1994, vol. 25B (2), pp. 227-33.
6. A. Theodorakakos and G. Bergeles: "Numerical Investigation of the Interface in a Continuous Steel Casting Mold Water Model", *Metallurgical and Materials Transactions B,* 1998, vol. 29B (6), pp. 1321-27.
7. J. Herbertson, Q.L. He, P.J. Flint and R.B. Mahapatra: "Modeling of Metal Delivery to Continuous Casting Moulds", in *Steelmaking Conf. Proceedings*, vol. 74, ISS, Warrendale, PA, 1991, pp. 171-85.
8. G.D. Lawson, S.C. Sander, W.H. Emling, A. Moitra and B.G. Thomas: "Prevention of Shell Thinning Breakouts Associated with Widening Width Changes", in *Steelmaking Conference Proceedings*, vol. 77, Iron and Steel Society, 1994, pp. 329-36.
9. R. Bommaraju, R. Glennon and M. Frazee: "Analysis of the Cause and Prevention of Longitudinal Midface Cracks and Depressions on Continuously Cast Free-Machining Steel Blooms", in *Continuous Casting Vol. 9*, M. Wolf, ed., ISS, Warrendale, PA, 1997, pp. 307-18.
10. B.G. Thomas, D. Lui and B. Ho: "Effect of Transverse and Oscillation Marks on Heat Transfer in the Continuous Casting Mold", in *Applications of Sensors in Materials Processing*, V. Viswanathan, ed., TMS, Warrendale, PA, 1997, pp. 117-42.
11. T.J.H. Billany, A.S. Normanton, K.C. Mills and P. Grieveson: "Surface Cracking in Continuously Cast Products", *Ironing and Steelmaking*, 1991, vol. 18, pp. 403-10.
12. W.H. Emling, T.A. Waugaman, S.L. Feldbauer and A.W. Cramb: "Subsurface Mold Slag Entrainment in Ultra-Low Carbon Steels", in *Steelmaking Conference Proceedings*, vol. 77, (Chicago, IL, April 13-16, 1997), ISS, Warrendale, PA, 1994, pp. 371-79.
13. J. Knoepke, M. Hubbard, J. Kelly, R. Kittridge and J. Lucas: "Pencil Blister Reduction at Inland Steel Company", in *Steelmaking Conference Proceedings*, vol. 77, (Chicago, IL, March 20-23, 1994), ISS, Warrendale, PA, 1994, pp. 381-88.

14. J. Szekely and R.T. Yadoya: "The Physical and Mathematical Modeling of the Flow Field in the Mold Region of Continuous Casting Systems. Part II. The Mathematical Representation of the Turbulence Flow Field", *Metall. mater. trans.,* 1973, vol. 4, pp. 1379-88.
15. S.K. Choudhary and D. Mazumdar: "Mathematical Modeling of Transport Phenomena in Continuous Casting of Steel", *ISIJ Int.,* 1994, vol. 34 (7), pp. 584-92.
16. S.K. Choudhary and D. Mazumdar: "Mathematical Modeling of Fluid Flow, Heat Transfer and Solidification Phenomena in Continuous Casting of Steel", *Steel Res.,* 1995, vol. 66 (5), pp. 199-205.
17. B.G. Thomas and L.M. Mika: "Simulation of Heat Transfer and Fluid Flow Inside a Continuous Slab Casting Machine", *Second FIDAP Users Conference*, M. Engelman, ed., (Evanstan, IL), Fluid Dynamics International Inc., 500 Davis Ave., Suite 400, Evanston, IL, 1988, pp. 1-29.
18. B.G. Thomas, F.M. Najjar and L.J. Mika: "The Removal of Superheat from Continuous Casting Molds", *Proc. F.Weinberg Int. Symposium on Solidification Processing, 29th Canadian Inst. Min. Met. Conf.*, J.E. Lait and I.V. Samarasekera, eds., (Hamilton, Ontario), Pergamon Press, Inc., Toronto, 1990, pp. 131-45.
19. B.G. Thomas, L.M. Mika and F.M. Najjar: "Simulation of Fluid Flow Inside a Continuous Slab Casting Machine", *Metall. Trans. B,* 1990, vol. 21B, pp. 387-400.
20. B.G. Thomas and F.M. Najjar: "Finite-Element Modeling of Turbulent Fluid Flow and Heat Transfer in Continuous Casting", *Applied Mathematical Modeling,* 1991, vol. 15, pp. 226-43.
21. B.G. Thomas, Q. Yuan, S. Sivaramakrishnan, T. Shi, S.P. Vanka and M.B. Assar: "Comparison of four Methods to Evaluate Fluid Velocities in a Continuous Casting Mold", *ISIJ International,* 2001, vol. 41 (10), pp. 1262-71.
22. B.G. Thomas and L. Zhang: "Mathematical Modeling of Fluid Flow in Continuous Casting", *ISIJ International,* 2001, vol. 41 (10), pp. 1181-93.
23. X. Huang and B.G. Thomas: "Modeling Transient Flow Phenomena in Continuous Casting of Steel", in *35th Conference of Metallurgists*, vol. 23B, C. Twigge-Molecey, ed., CIM, 1996, pp. 339-56.
24. S. Sivaramakrishnan, H. Bai, B.G. Thomas, P. Vanka, P. Dauby and M. Assar: "Transient Flow Structures in Continuous Cast Steel", in *Ironmaking Conference Proceedings*, vol. 59, ISS, Warrendale, PA, 2000, pp. 541-57.
25. Q. Yuan, S.P. Vanka and B.G. Thomas: "Large Eddy Simulations of Turbulent Flow and Inclusion Transport in Continuous Casting of Steel", *2nd International Symposium on Turbulent and Shear Flow Phenomena*, (Stockholm, Sweden), Royal Insitute of Technology(KTH), 2001, p. 6.
26. K. Takatani, Y. Tanizawa, H. Mizukami and K. Nishimura: "Mathematical Model for Transient Fluid Flow in a Continuous Casting Mold", *ISIJ International,* 2001, vol. 41 (10), pp. 1252-61.
27. R. Sobolewski and D.J. Hurtuk: "Water Modeling of Slab Caster Flow Conditions", *2nd Process Technology Conf. Proc.*, Iron and Steel Society, Warrendale, PA, 1982, vol. 2, pp. 160-65.
28. B.G. Thomas, X. Huang and R.C. Sussman: "Simulation of Argon Gas Flow Effects in a Continuous Slab Caster", *Metall. Trans. B,* 1994, vol. 25B (4), pp. 527-47.
29. D. Gupta and A.K. Lahiri: "A Water Model Study of the Flow Asymmetry Inside a Continuous Slab Casting Mold", *Metallurgical and Materials Transactions B,* 1996, vol. 27B (5), pp. 757-64.

30. D. Gupta, S. Chakraborty and A.K. Lahiri: "Asymmetry and Oscillation of the Fluid Flow Pattern in a Continuous Casting Mould: a Water Model Study", *ISIJ Int.,* 1997, vol. 37 (7), pp. 654-58.
31. S. Sivaramakrishnan, B.G. Thomas and S.P. Vanka: "Large Eddy Simulation of Turbulent Flow in Continuous Casting of Steel", in *Materials Processing in the Computer Age*, vol. 3, V. Voller and H. Henein, eds., TMS, Warrendale, PA, 2000, pp. 189-98.
32. M.B. Assar, P.H. Dauby and G.D. Lawson: "Opening the Black Box: PIV and MFC Measurements in a Continuous Caster Mold", in *Steelmaking Conference Proceedings*, vol. 83, ISS, Warrendale, PA, 2000, pp. 397-411.
33. J. Smagorinsky: "General Circulation Experiments With the Primitive Equations, I. The Basic Experiment", *Monthly Weather Review,* 1963, vol. 91, pp. 99-164.
34. Q. Yuan, B. Zhao, S.P. Vanka and B.G. Thomas: "Study of Computational Issues in Simulation of Transient Flow in Continuous Casting", *in preparation for Steel Research International,* 2004.
35. F.H. Harlow and J.E. Welch: "Numerical Calculation of Time Dependent Viscous Incompressible Flow of Fluid with Free Surface", *Physics of Fluids,* 1965, vol. 8 (112), pp. 2182-89.
36. J. Crank and P. Nicolson: "A Practical Method for Numerical Evaluation of Solutions of Partial Differential Equations of the Heat-Conduction Type", *Proc. Cambridge Philos. Soc.,* 1947, vol. 43, pp. 50-67.
37. L.F. Sampine and M.K. Gordon: *Computer Solution of Ordinary Differential Equations: the Initial Value Problem*, W.H. Freeman, ed. San Francisco, 1975.
38. W.H. Press, S.A. Teukolsky, W.T. Vetterling and B.P. Flannery: *Numerical Recipes: The Art of Scientific Computing*, Cambridge University Press, 1992, pp. 490-600.
39. *User's Manual: Hypre - High Performance Preconditioners*, Center for Applied Scientific Computing, Lawrence Livermore National Laboratory, Report No. UCRL-MA-137155 DR, 2001.
40. B.G. Thomas, R. O'Malley, T. Shi, Y. Meng, D. Creech and D. Stone: "Validation of Fluid Flow and Solidification Simulation of a Continuous Thin Slab Caster", in *Modeling of Casting, Welding, and Advanced Solidification Processes*, vol. IX, Shaker Verlag GmbH, Aachen, Germany, 2000, pp. 769-76.
41. Y. Meng and B.G. Thomas: "Heat Transfer and Solidification Model of Continuous Slab Casting: CON1D", *Metallurgical and Materials Transactions B,* 2003, vol. 34B (5), pp. 685-705.
42. B.G. Thomas, R.J. O'Malley and D.T. Stone: "Measurement of temperature, solidification, and microstructure in a continuous cast thin slab", *Modeling of Casting, Welding, and Advanced Solidification Processes*, B.G. Thomas and C. Beckermann, eds., (San Diego, CA), TMS, Warrendale, PA, 1998, vol. VIII, pp. 1185-99.
43. F.M. Najjar, B.G. Thomas and D.E. Hershey: "Turbulent Flow Simulations in Bifurcated Nozzles: Effects of Design and Casting Operation", *Metall. Trans. B,* 1995, vol. 26B (4), pp. 749-65.
44. H. Bai and B.G. Thomas: "Turbulent Flow of Liquid Steel and Argon Bubbles in Slide-Gate Tundish Nozzles, Part II, Effect of Operation Conditions and Nozzle Design", *Metallurgical and Materials Transactions B,* 2001, pp. 269-84.
45. B. Zhao, B.G. Thomas, S.P. Vanka and R.J. O'Malley: "Large Eddy Simulation of Transient Flow and Superheat Transport in Continuous Casting of Steel Slabs", *in preparation for Metallurgical & Materials Transactions B,* 2003.

46. K. Horiuti: "Large Eddy Simulation of Turbulent Channel Flow by One-Equation Modeling", *Journal of the Physical Society of Japan,* 1985, vol. 54 (8), pp. 2855-65.
47. I. Wygnanski and H. Fiedler: "Some Measurements in the Self-Preserving Jet", *J. of Fluid Mech.,* 1969, vol. 38 (577-612).
48. S. Sivaramakrishnan: *Transient Fluid Flow in the Mold and Heat Transfer Through the Molten Slag Layer in Continuous Casting of Steel*, M.S. Thesis, University of Illinois, 2000.
49. A. Cramb, Y. Chung, J. Harman, A. Sharan and I. Jimbo: "The Slag/Metal Interface and Associated Phenomena. A History of Pneumatic Steelmaking", *Iron and Steelmaker,* 1997, vol. 24 (3), pp. 77-83.
50. Q. Yuan, T. Shi, B.G. Thomas and S.P. Vanka: "Simulation of Fluid Flow in the Continuous Casting of Steel", *Proceedings: Computational Modeling of Materials, Minerals and Metals Processing*, TMS, ed., (Seattle, WA), TMS (The Materials, Minerals and Metals Society), 2001, pp. 491-500.
51. J. Anagnostopoulos and G. Bergeles: "Three-Dimensional Modeling of the Flow and the Interface Surface in a Continuous Casting Mold Model", *Metallurgical and Materials Transactions B,* 1999, vol. 30B (6), pp. 1095-105.
52. R.J. O'Malley: Mansfield, OH, private communication, 2003.
53. N.J. Lawson and M.R. Davidson: "Oscillatory Flow in a Physical Model of a Thin Slab Casting Mould with a Bifurcated Submerged Entry Nozzle", *Journal of Fluids Engineering,* 2002, vol. 124 (6), pp. 535-43.

## LIST OF FIGURES AND TABLES

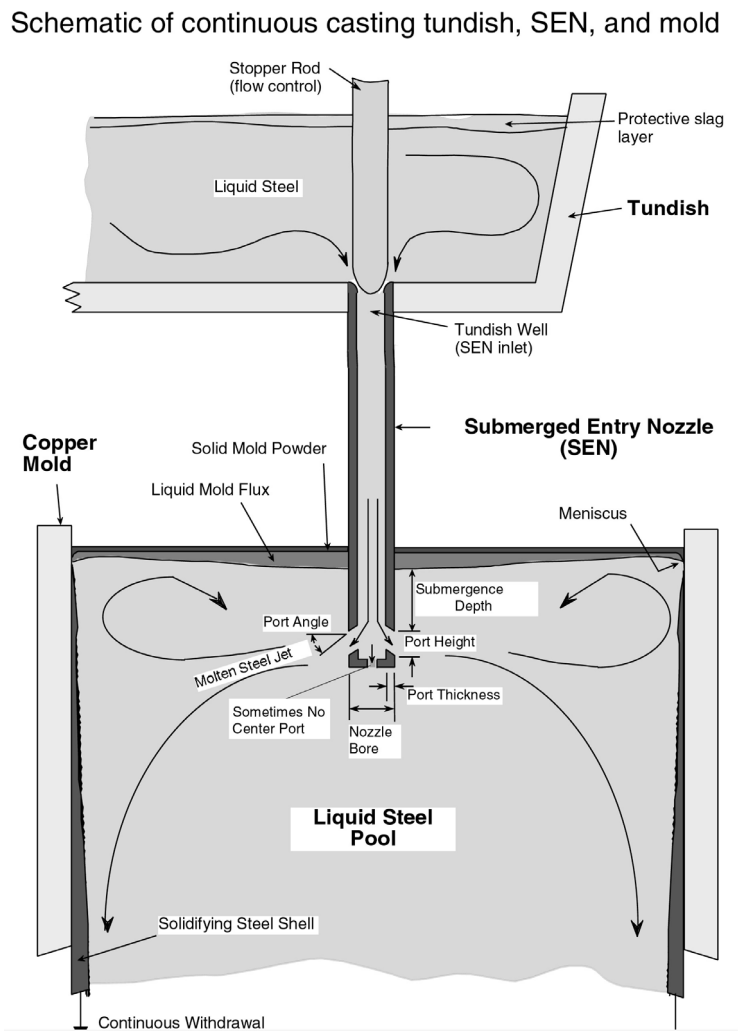


**Figure 1. Schematics of the process of continuous casting of steel.**

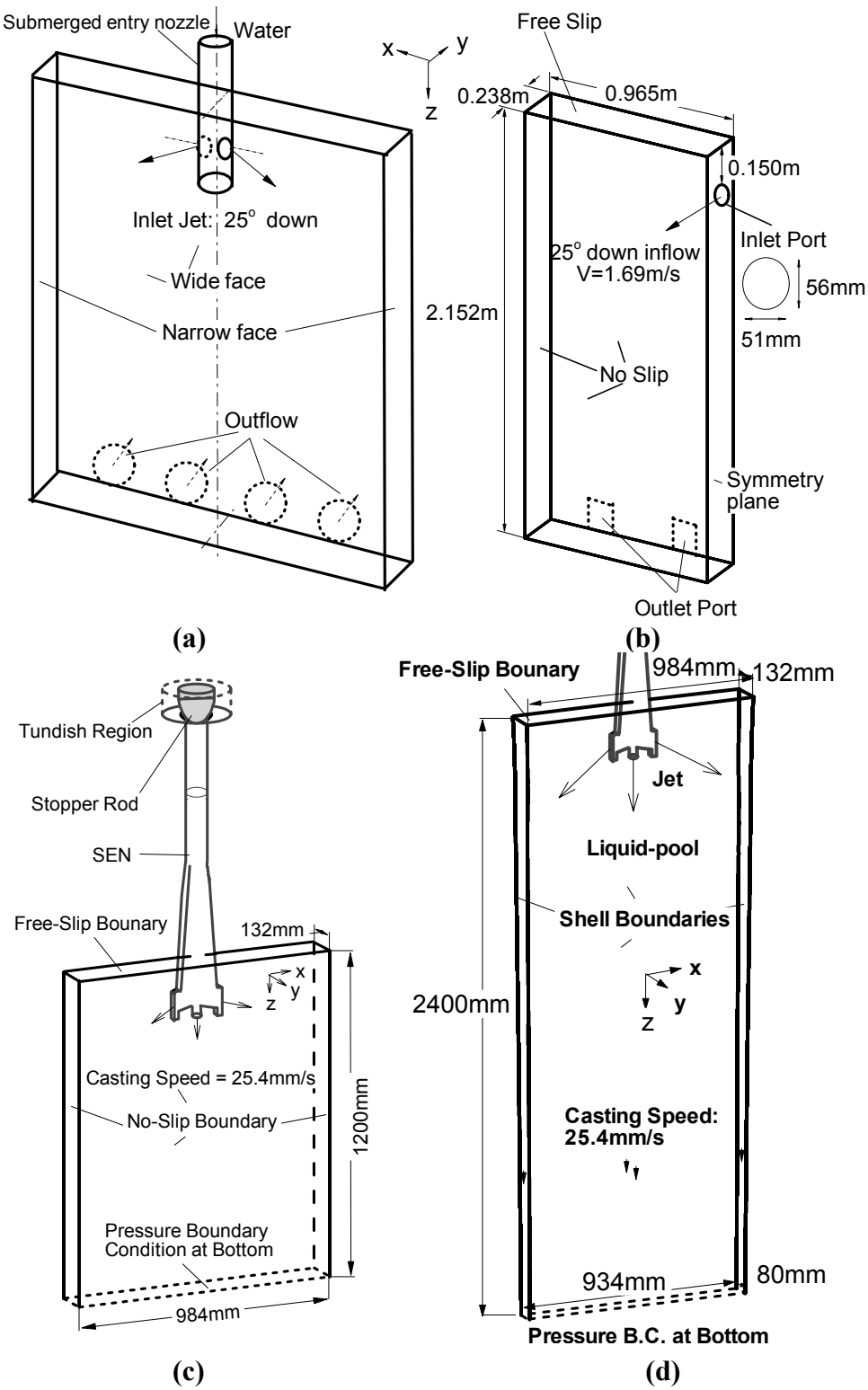


**Figure 2. Schematics of (a) the physical water model of *Case 1* and (b) its computational domain and the thin slab caster (c) *Case 2-W* and (d) *Case 2-S.***

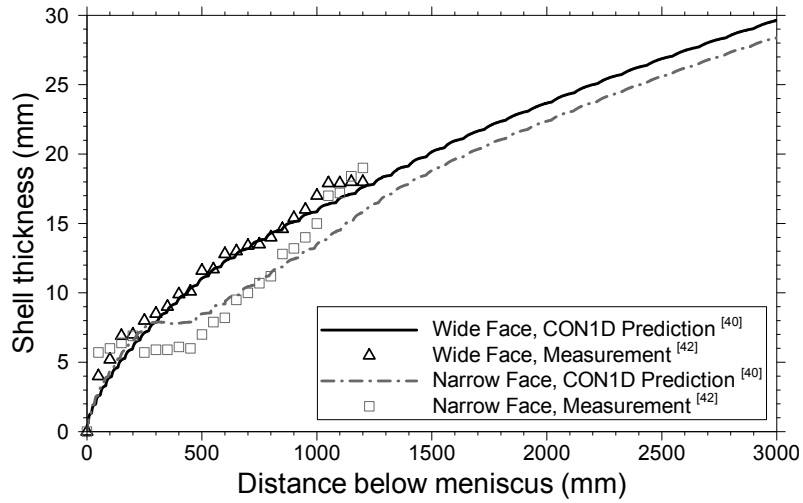


**Figure 3**. **Predicted steel shell thickness of *Case2-S* using CON1D,** [40, 41] **compared with measurements.** [42]

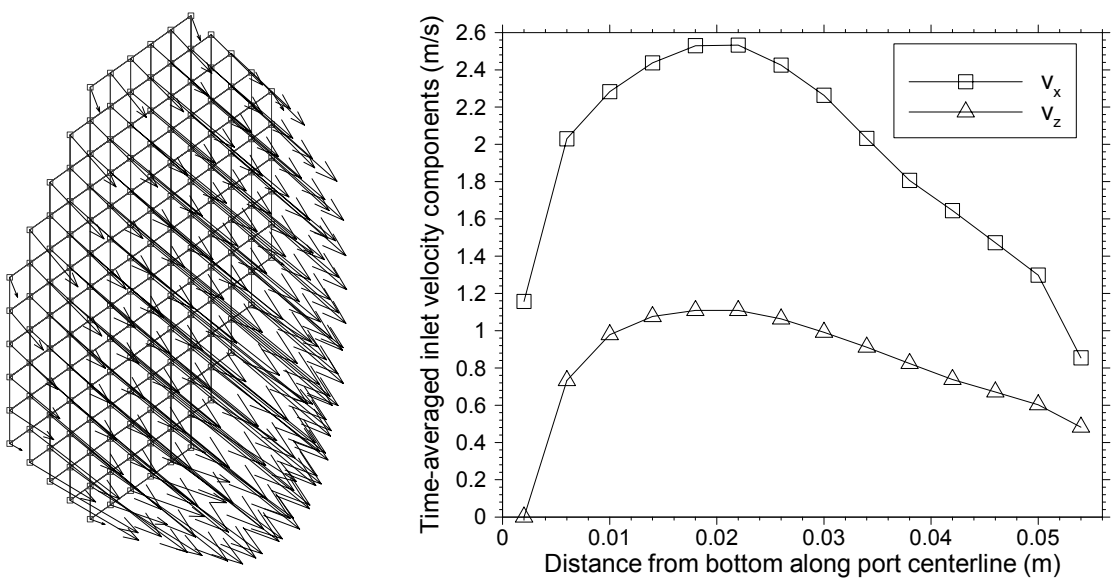


**(a)** **(b)**

**Figure 4. Inlet velocities of the standard slab caster water model:**

**(a) time-averaged velocity vectors at the inlet port and**

**(b) transverse (x) and downward (z) velocity components along nozzle port centerline.**

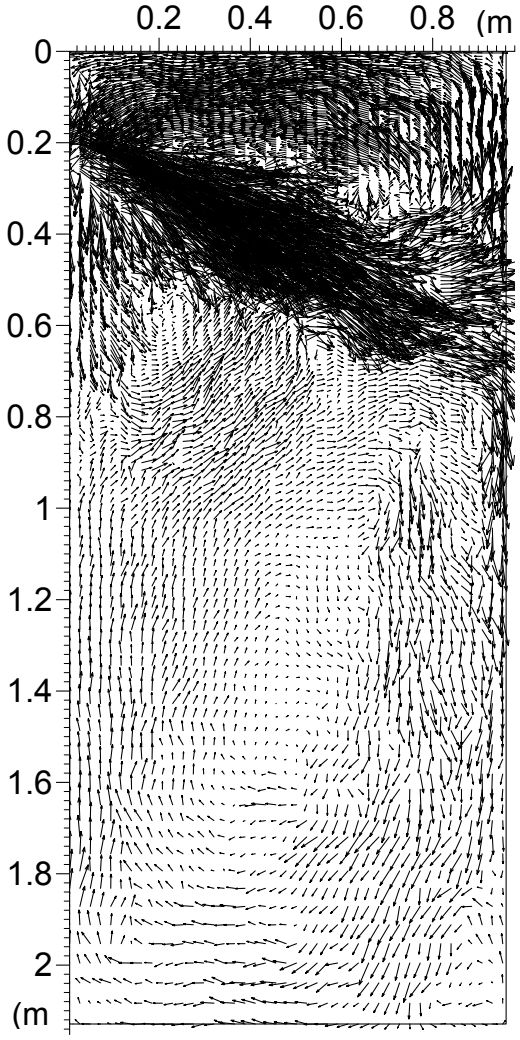


(Scale : → 0.25 m/s)

**Figure 5**. **Typical instantaneous velocity vector plot at the center plane between wide faces (*Case 1*), obtained from simulation.**

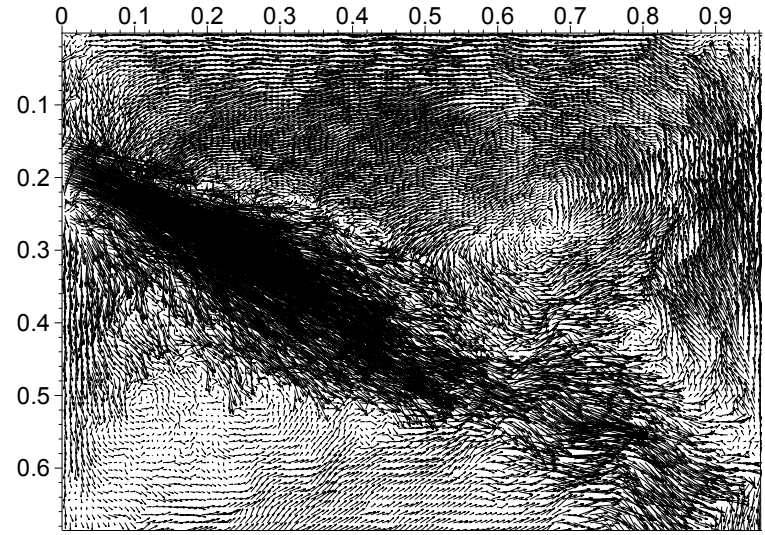


(Scale : → 0.25m/s)

**(a)**

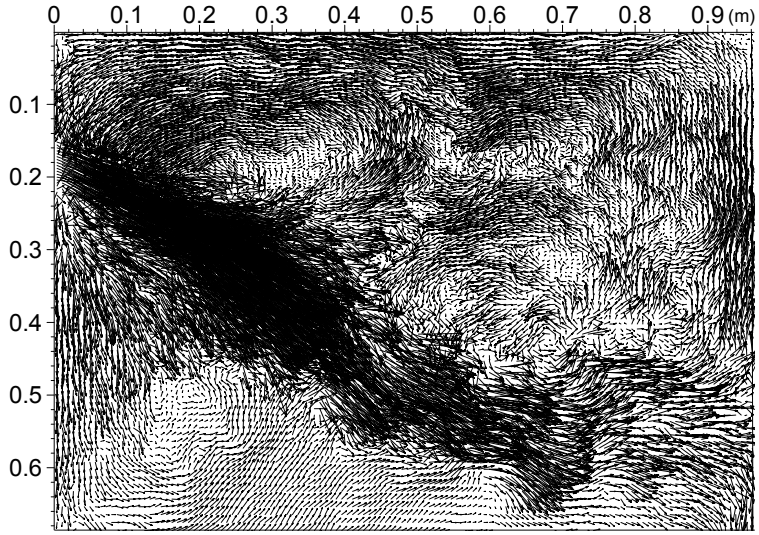


**(b)**

**Figure 6**. **Predicted chaotic flow patterns in the upper recirculation zone (*Case 1*)**

**(a) simple vortices and (b) complex multiple vortices**.

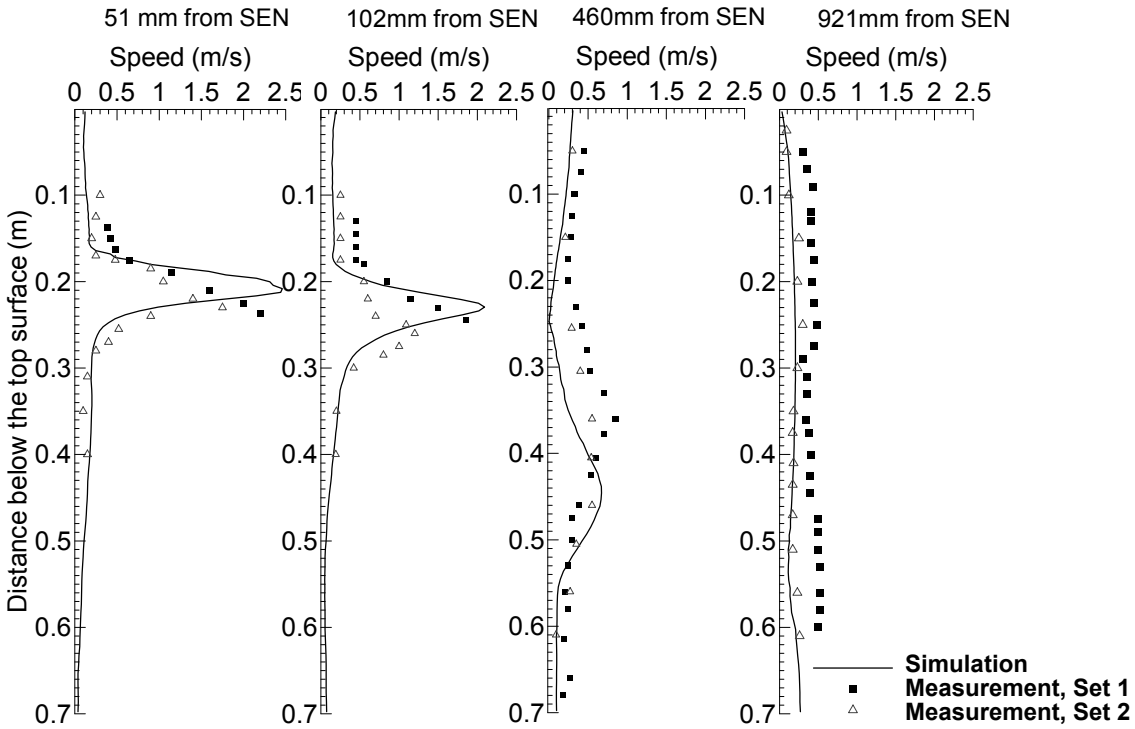


**Figure 7. Comparison of the prediction and measurement of the time-averaged speed $(v_x^2+v_z^2)^{1/2}$ along four vertical lines at different distances from SEN(*Case 1*).**

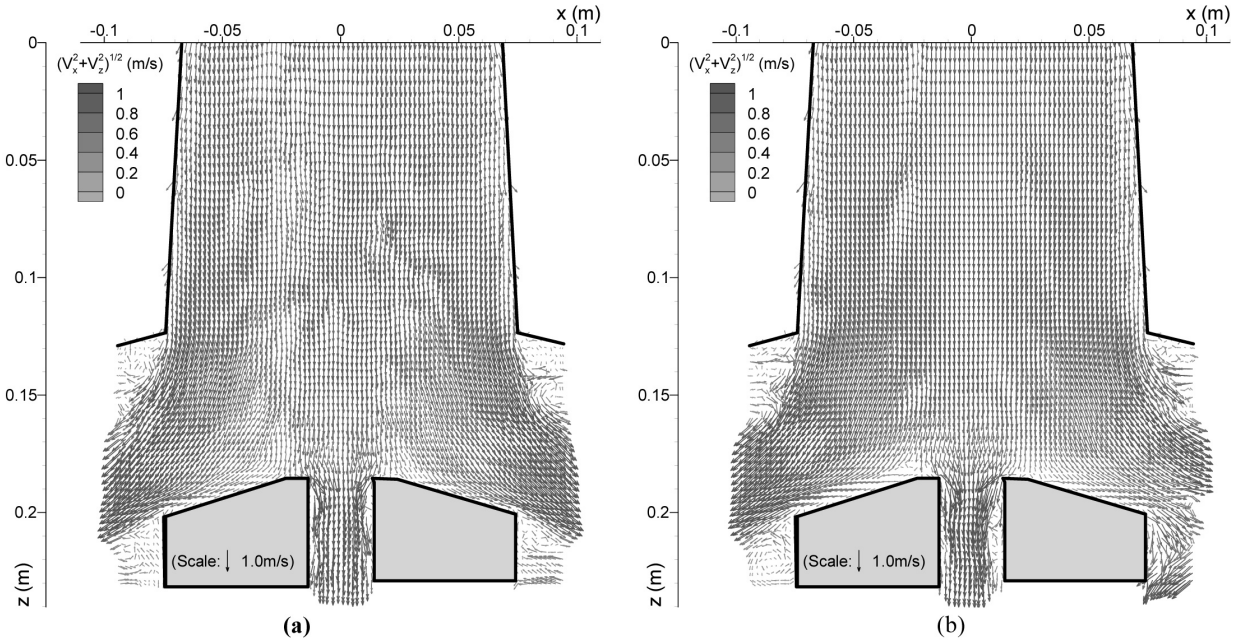


**Figure 8. Typical instantaneous velocity fields near nozzle ports at the center plane between wide faces, obtained from a large eddy simulation of the nozzle (*Case2-W & 2-S*).**

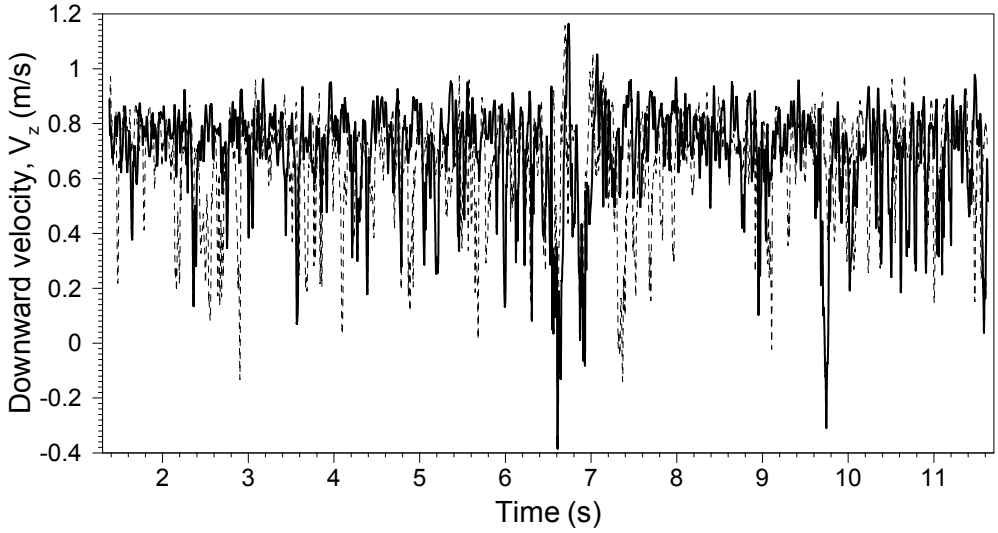


**Figure 9. Time variation of downward velocity ($v_z$) at two symmetrical points on the side nozzle ports.**

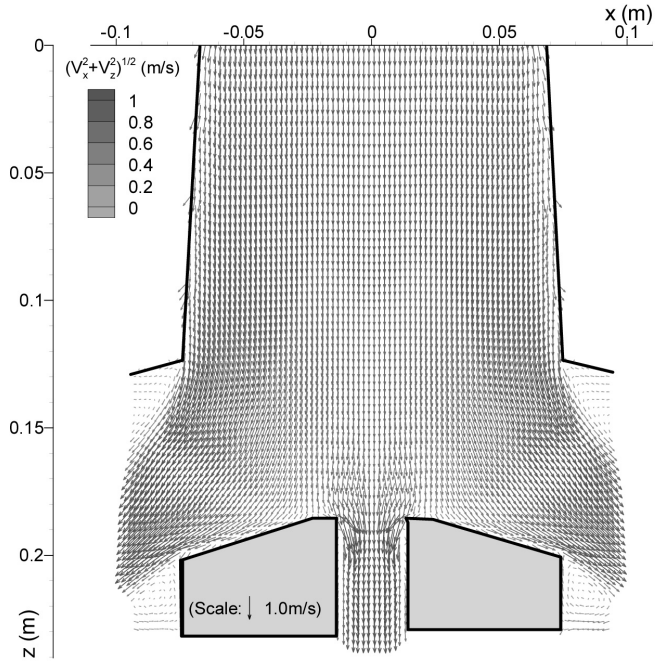


**Figure 10. Time-averaged velocity fields near nozzle ports at the center plane between narrow faces, obtained from the simulation (*Case 2-W* & *2-S*).**

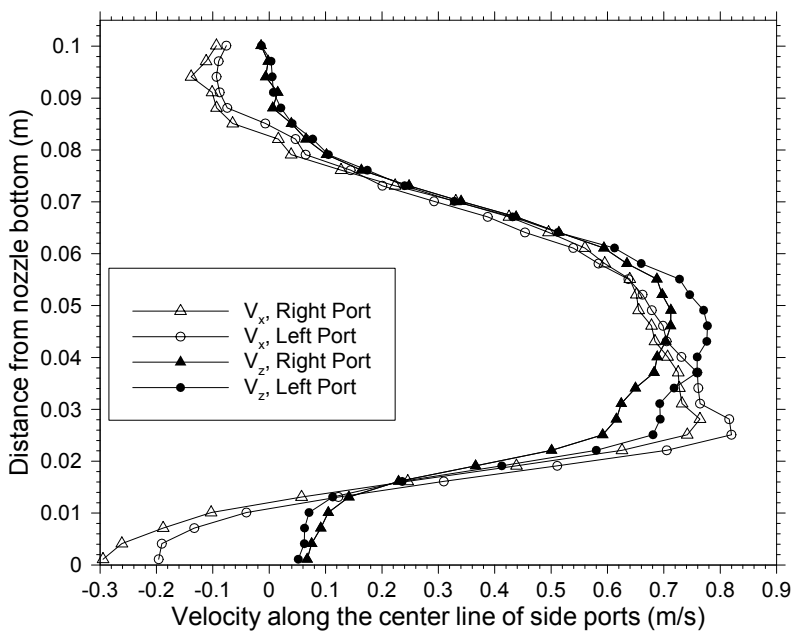


**Figure 11. Time-averaged velocities along the nozzle port centerline on both sides.**

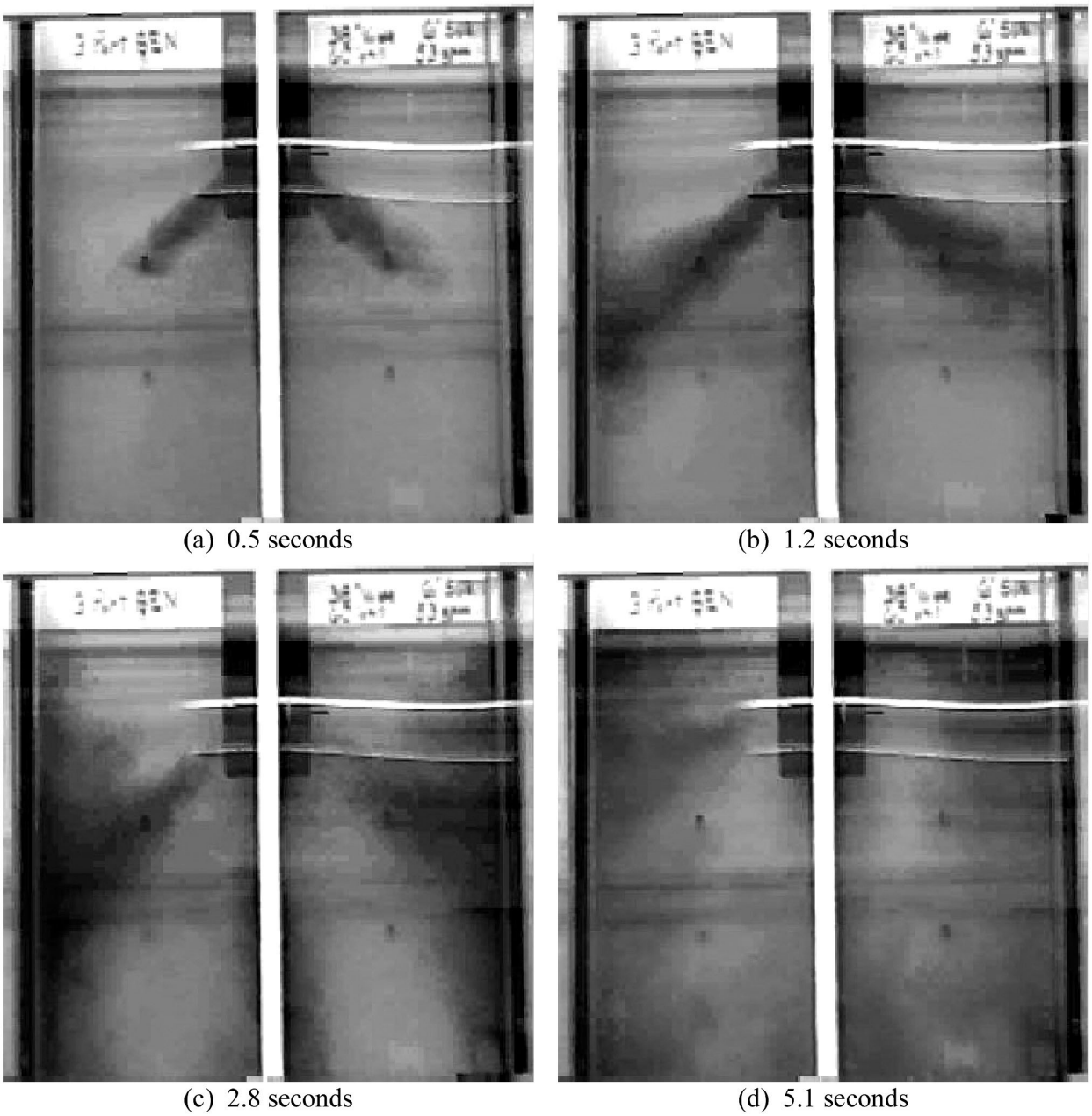

(a) 0.5 seconds (b) 1.2 seconds

(c) 2.8 seconds (d) 5.1 seconds

**Figure 12. Dye injection experiment of *Case 2-W* at four instants**.

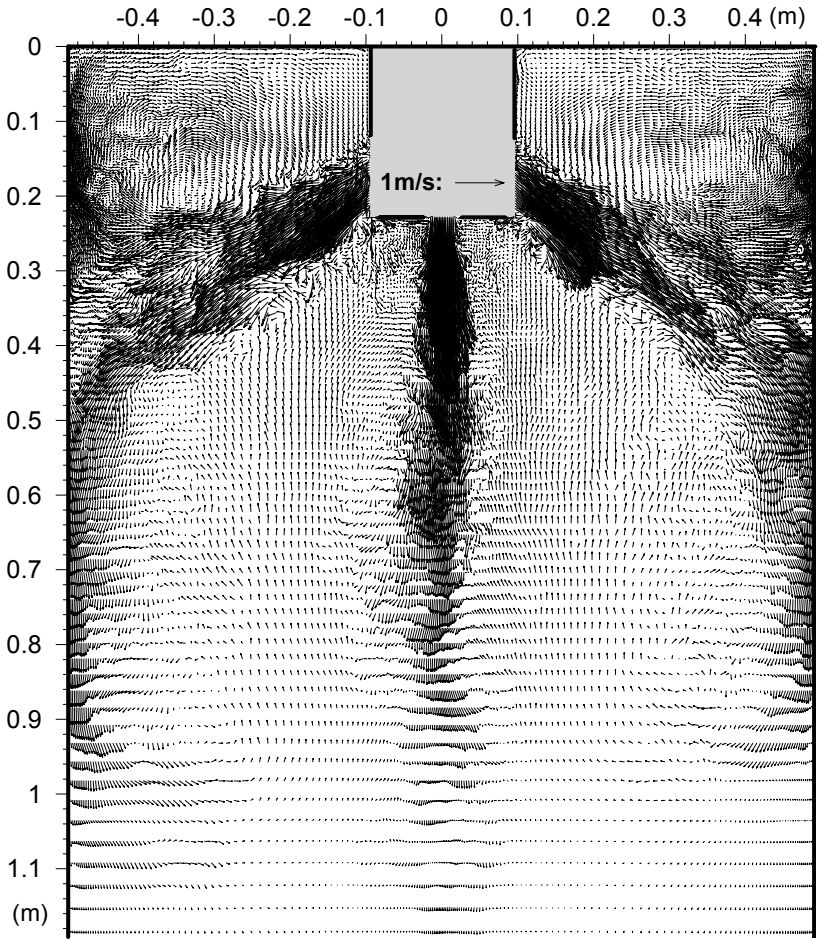


**Figure 13. Typical instantaneous velocity vector plot at the center plane between wide faces (*Case 2-W*), obtained from simulation.**

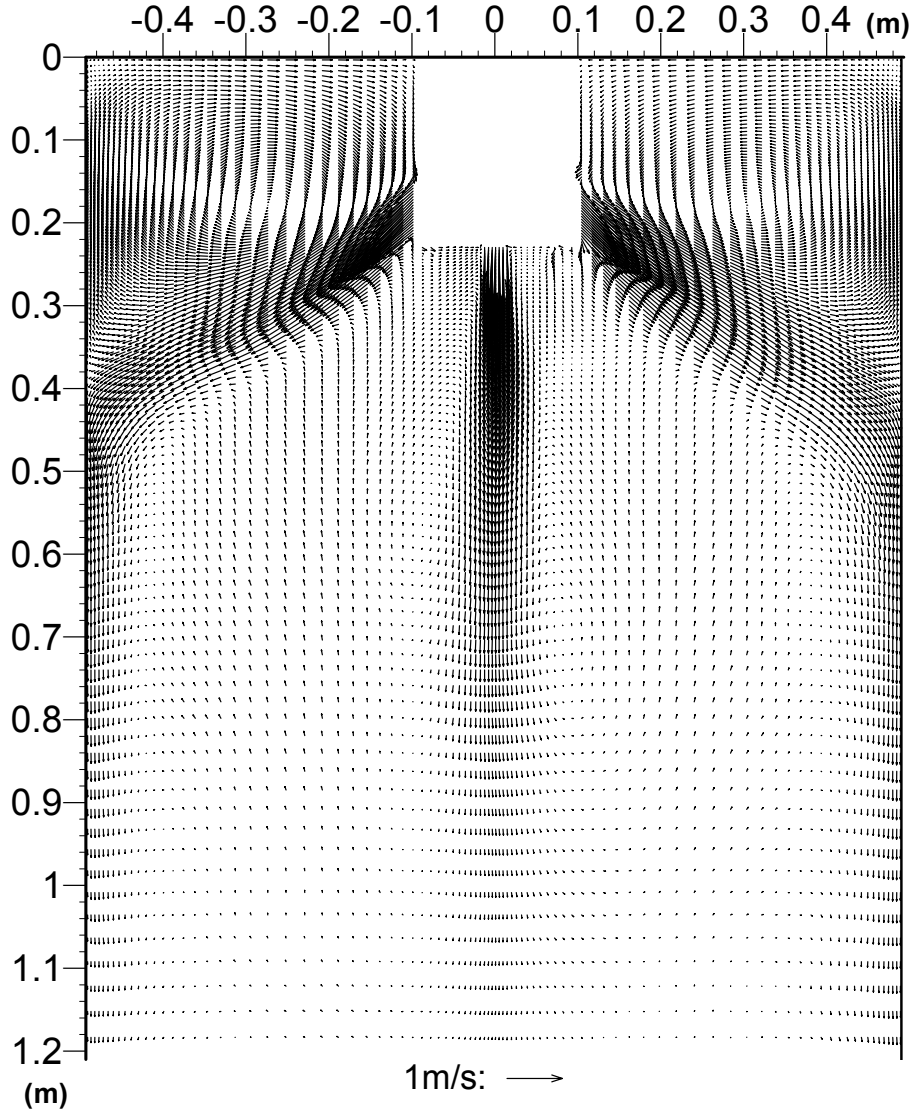


**Figure 14. Time-averaged velocity vector plot at the center plane between wide faces (*Case 2-W*), obtained from simulation.**

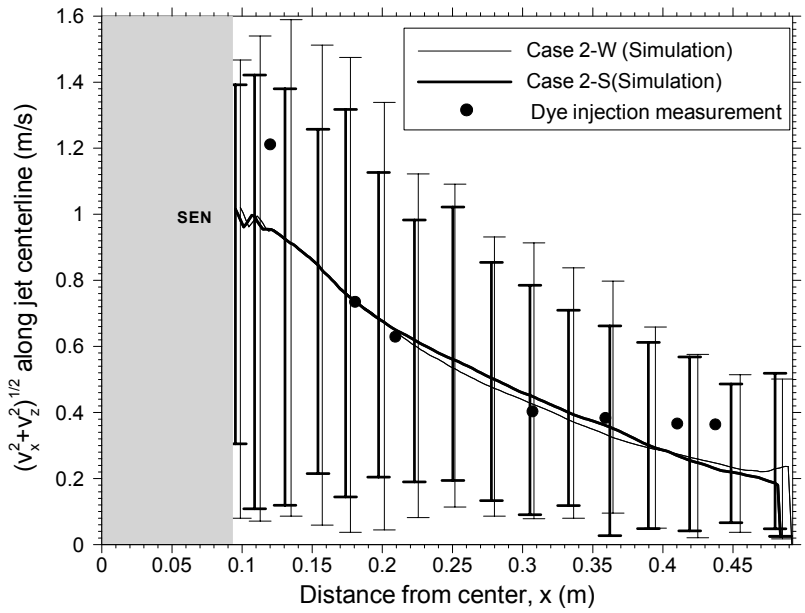


**Figure 15. Comparison of time-averaged speed $(v_x^2+v_z^2)^{1/2}$ along side jet centerline between computation and dye injection estimate (*Case 2-W*).**

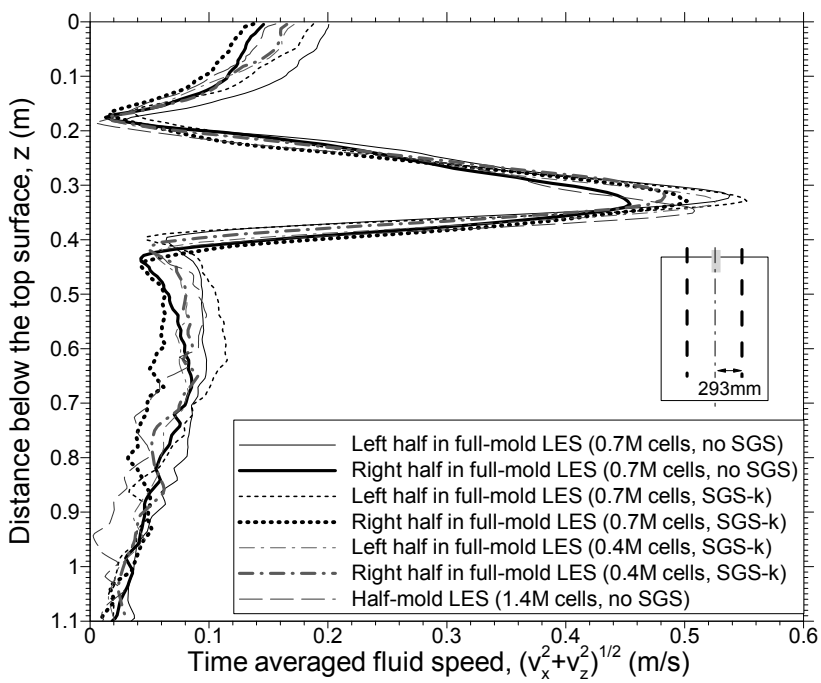


**Figure 16. Comparison of computed fluid speeds $(v_x^2+v_z^2)^{1/2}$ along the vertical line in the center plane, obtained from three different grid resolutions (*Case 2-W*).**

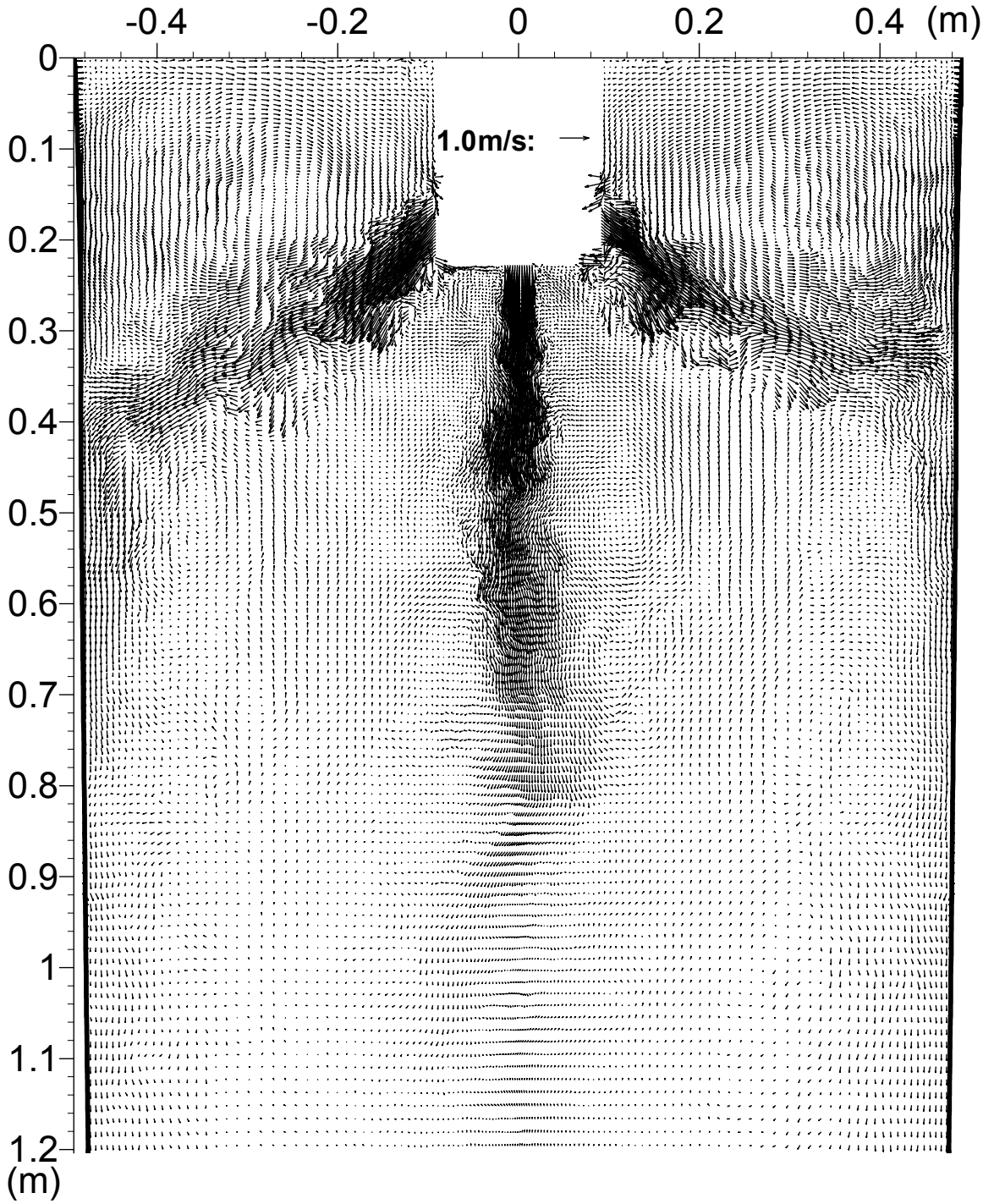


**Figure 17. Typical instantaneous velocity vector plot at the center plane between wide faces (*Case 2-S*), obtained from simulation.**

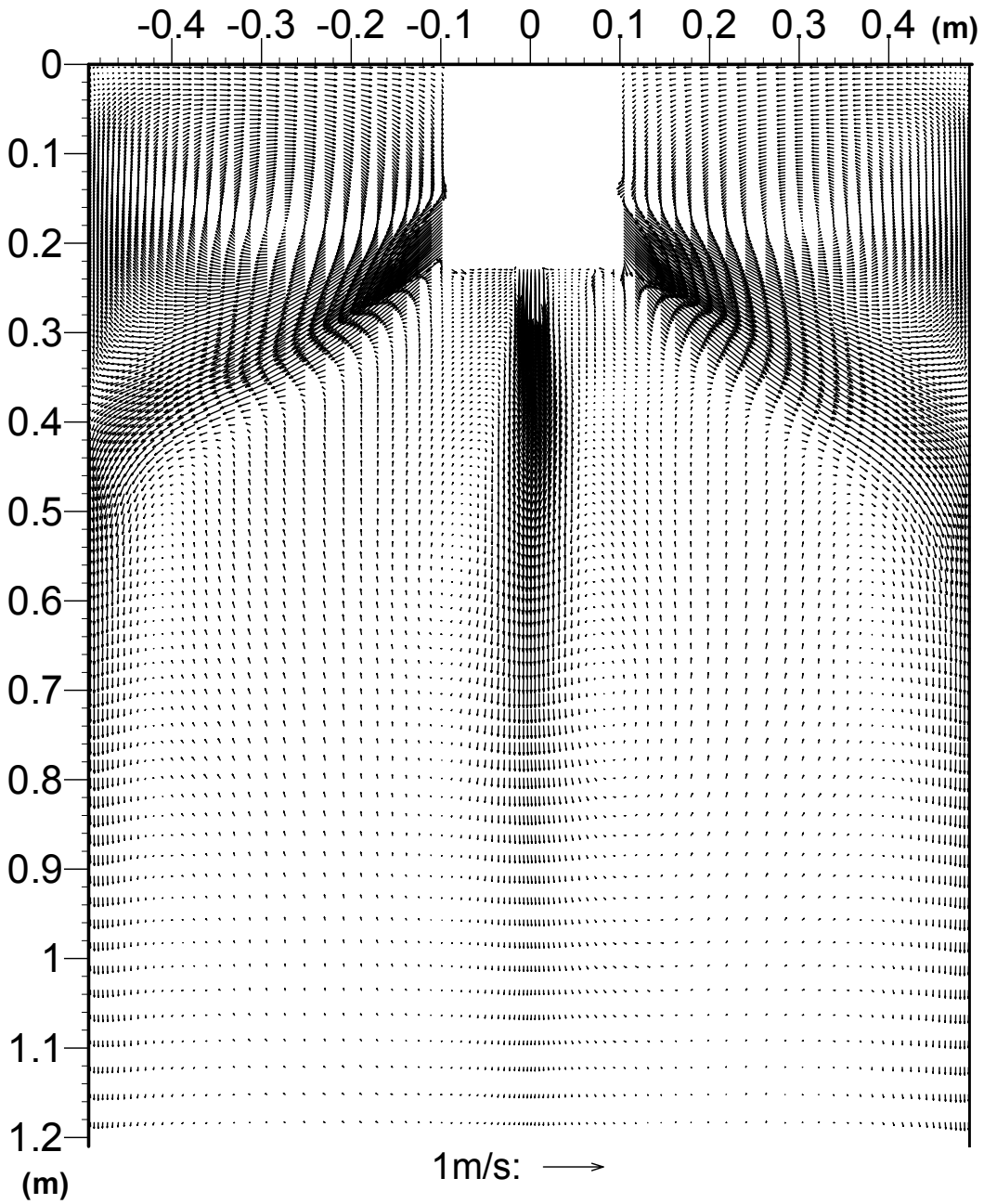


**Figure 18. Time-averaged velocity vectors at the center plane between wide faces (*Case 2-S*), obtained from simulation.**

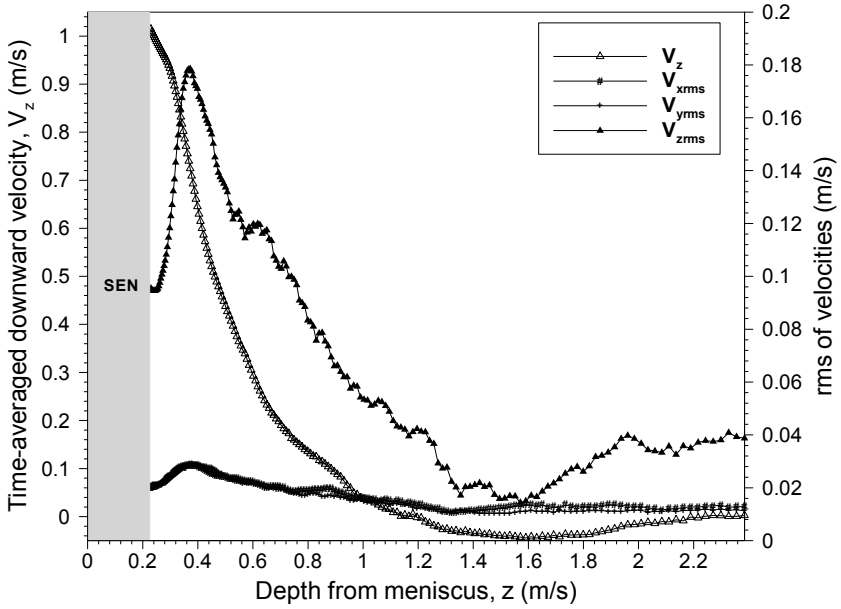


**Figure 19. Time averaged and *rms* values of velocities along the center jet centerline (*Case2-S*).**

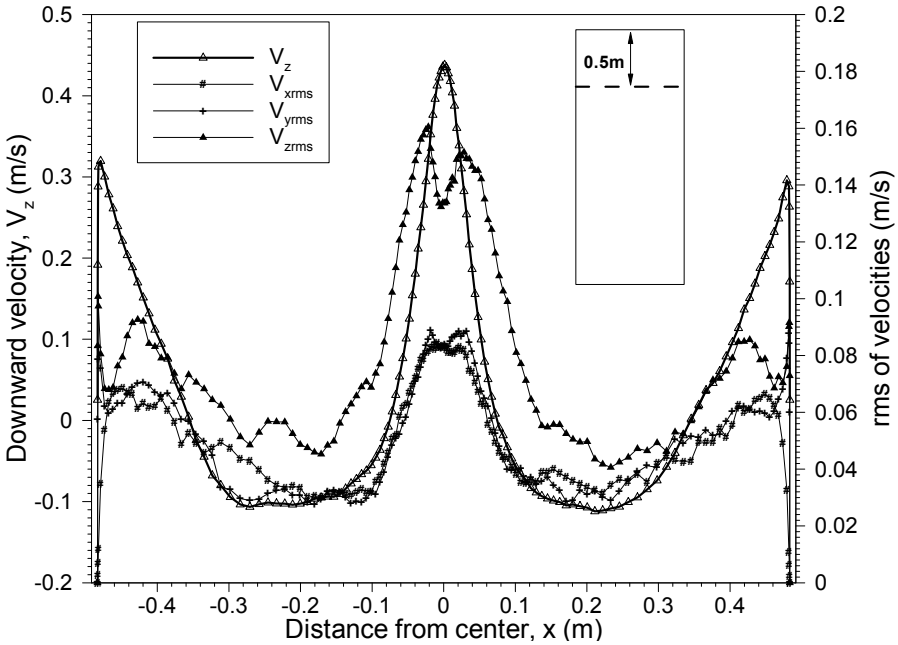


**Figure 20. Time averaged and *rms* values of velocities along a horizontal line 0.5m below meniscus half way between wide faces (*Case2-S*).**

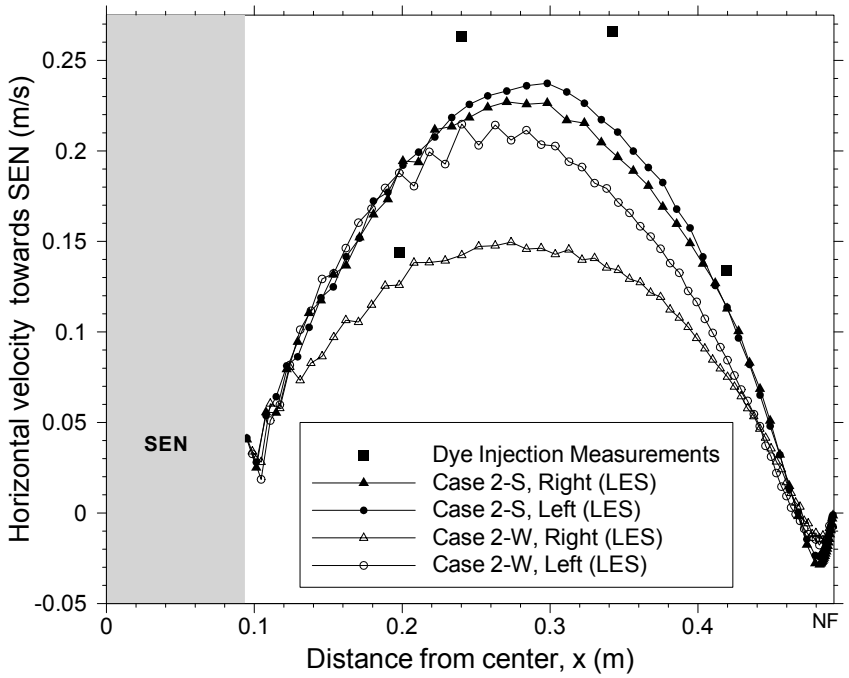


**Figure 21. Comparison of time-averaged horizontal velocity towards SEN along top surface centerline between *Case 2-W* and *Case 2-S*.**

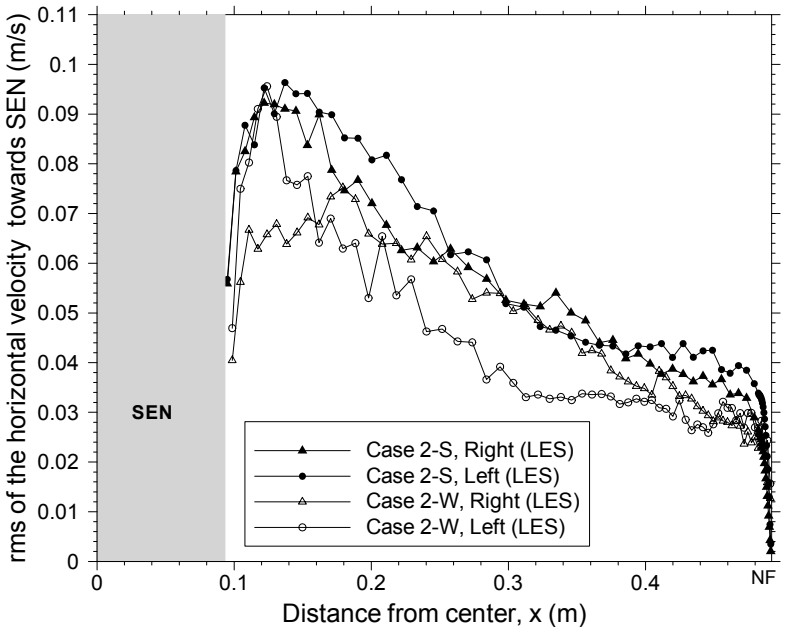


**Figure 22. Comparison of the *rms* values of the velocity in Fig. 21.**

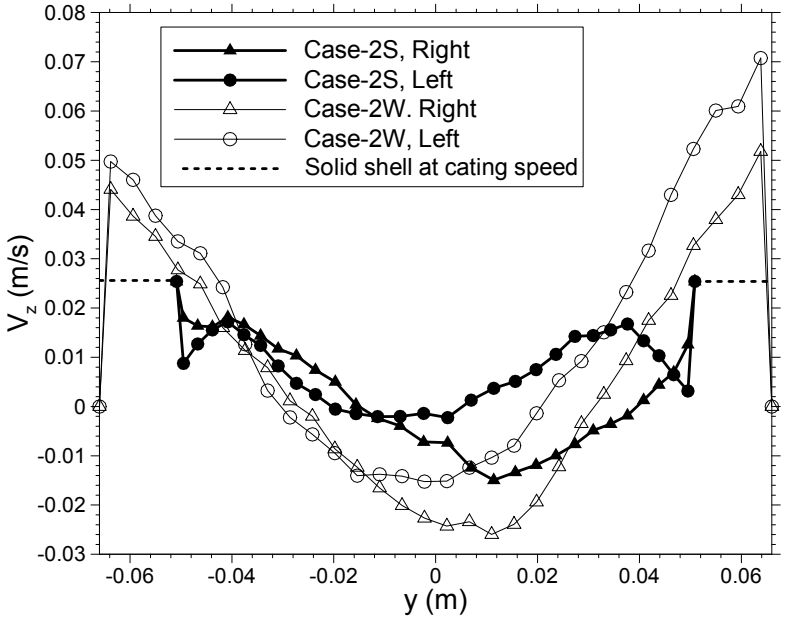


**Figure 23. Comparison of the time-averaged downward velocity between *Case 2-W* and *Case 2-S* in the lower recirculation zones.**

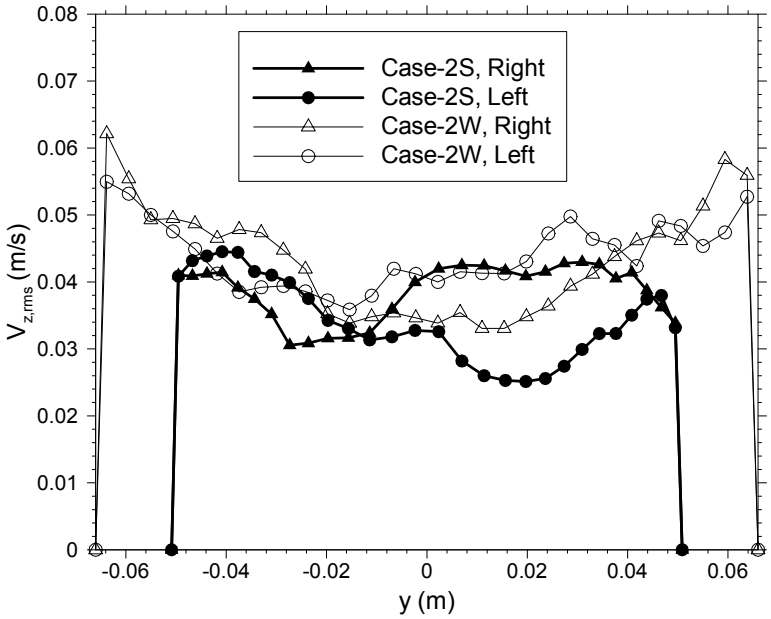


**Figure 24. Comparison of the *rms* values of the velocity in Fig. 23.**

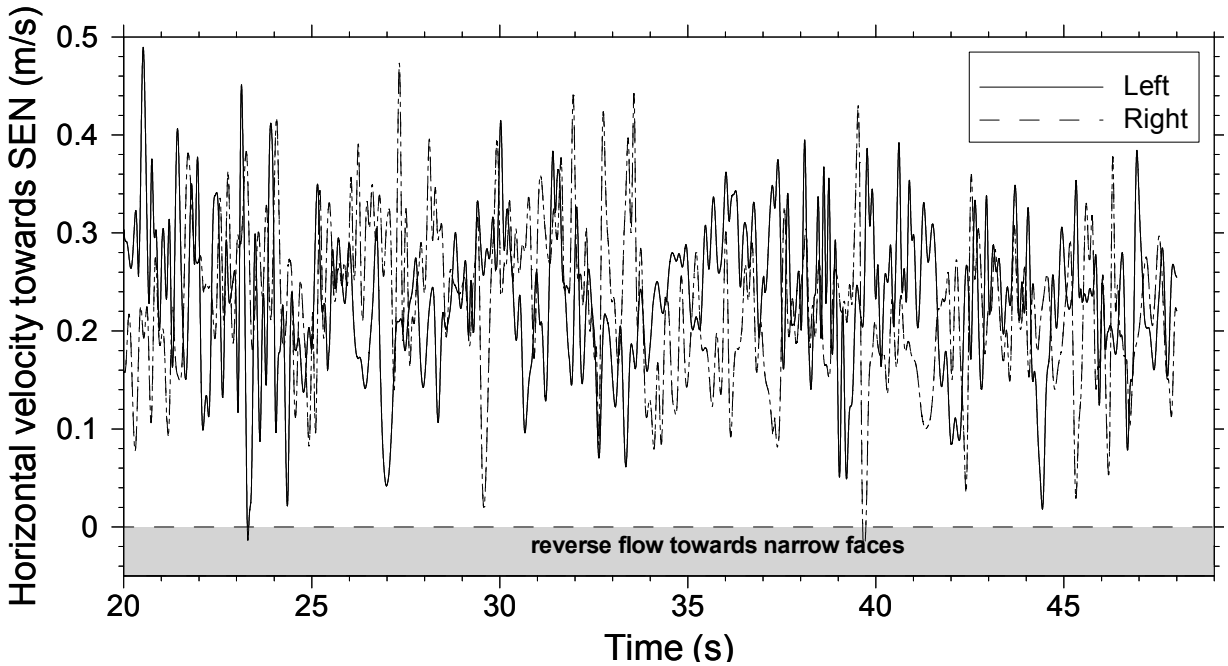


**(a)**

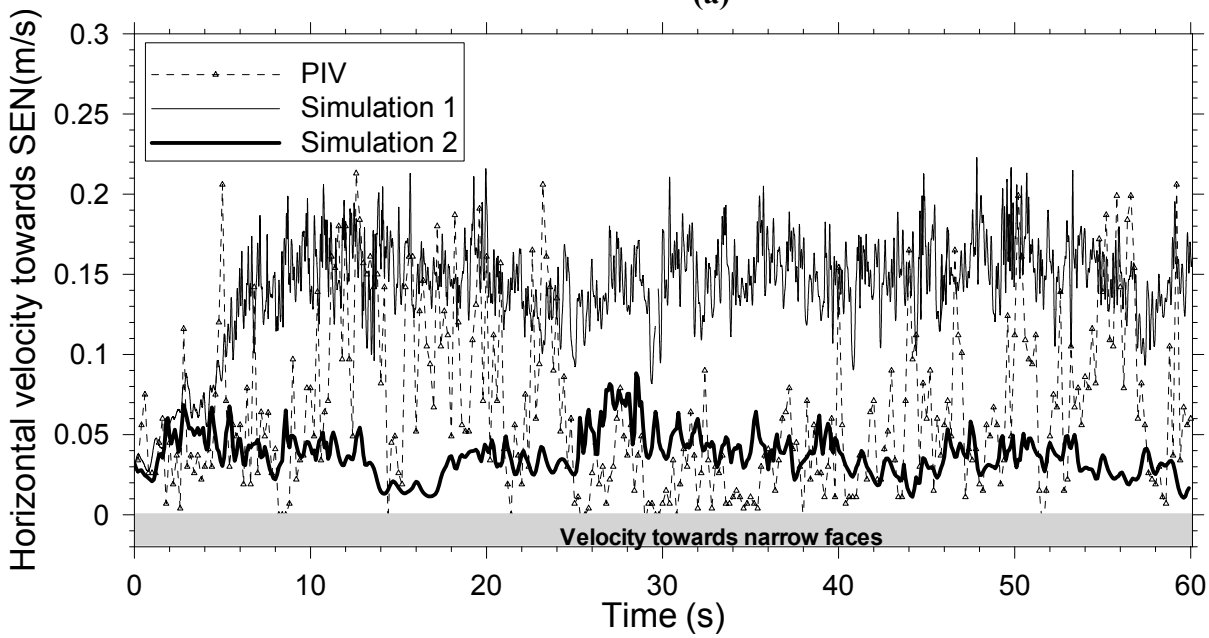


**(b)**

**Figure 25. Time variations of the horizontal velocity towards SEN at the center point of the top surface: (a) *Case 2-S* and (b) a 0.4-scale water model.** [24]

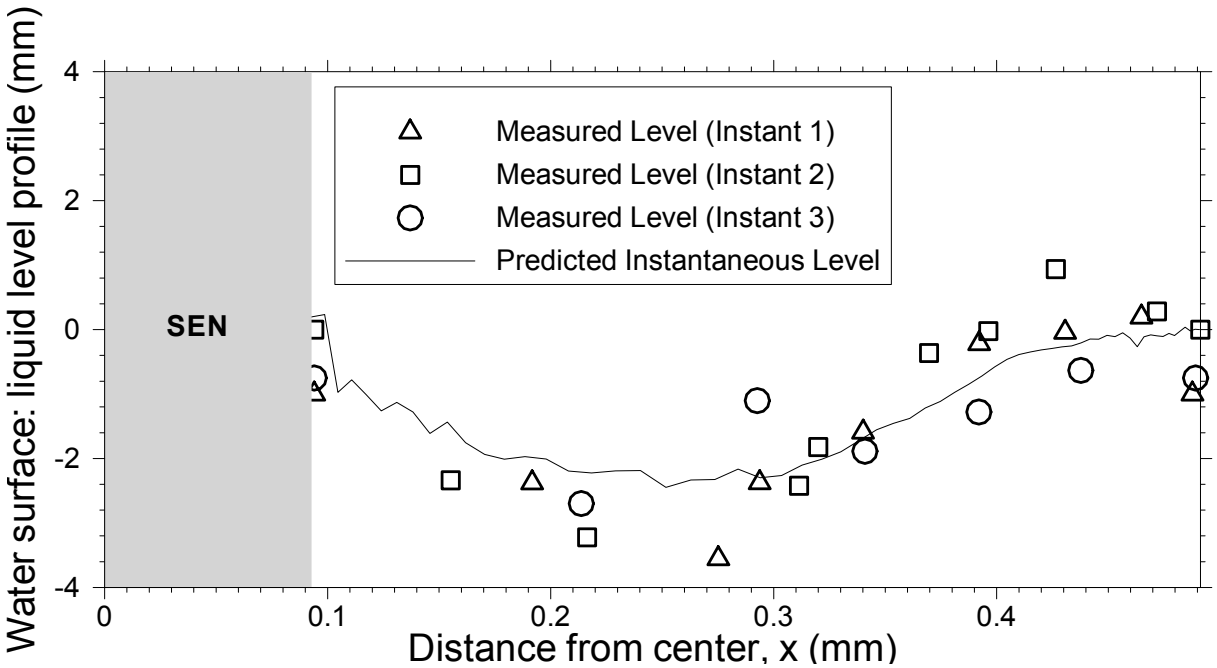


**(a)**

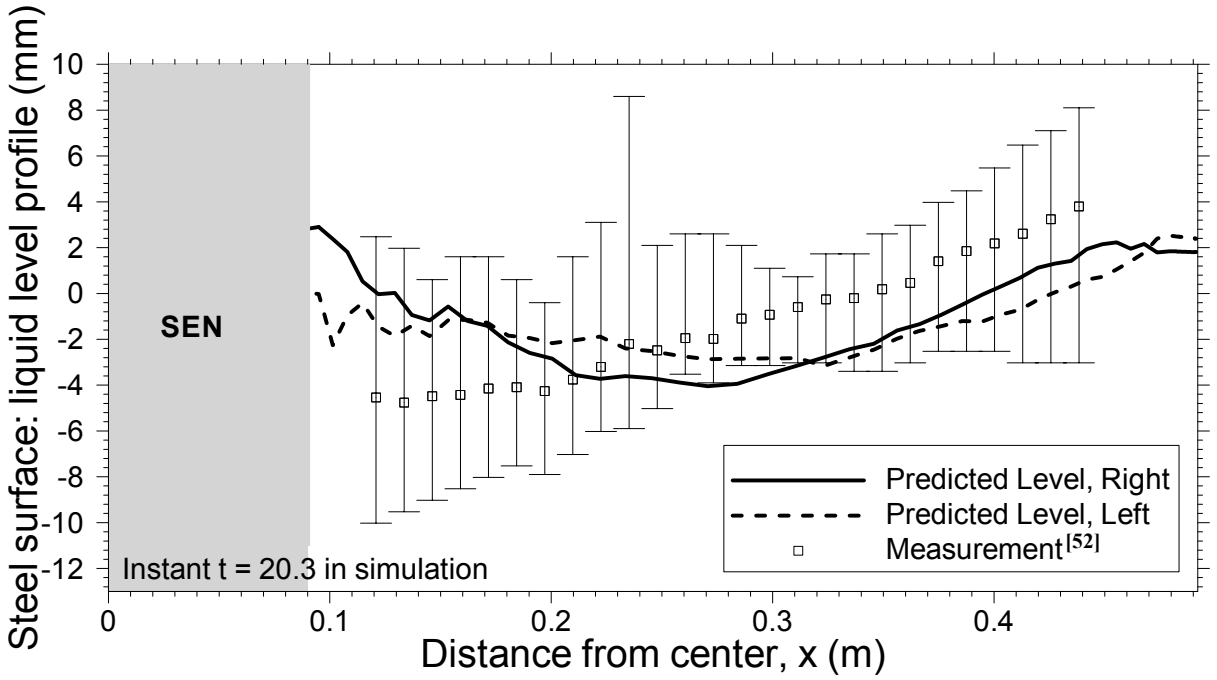


**(b)**

**Figure 26. Comparison of predicted and measured top surface liquid levels in (a) *Case 2-W* and (b) *Case 2-S*.**

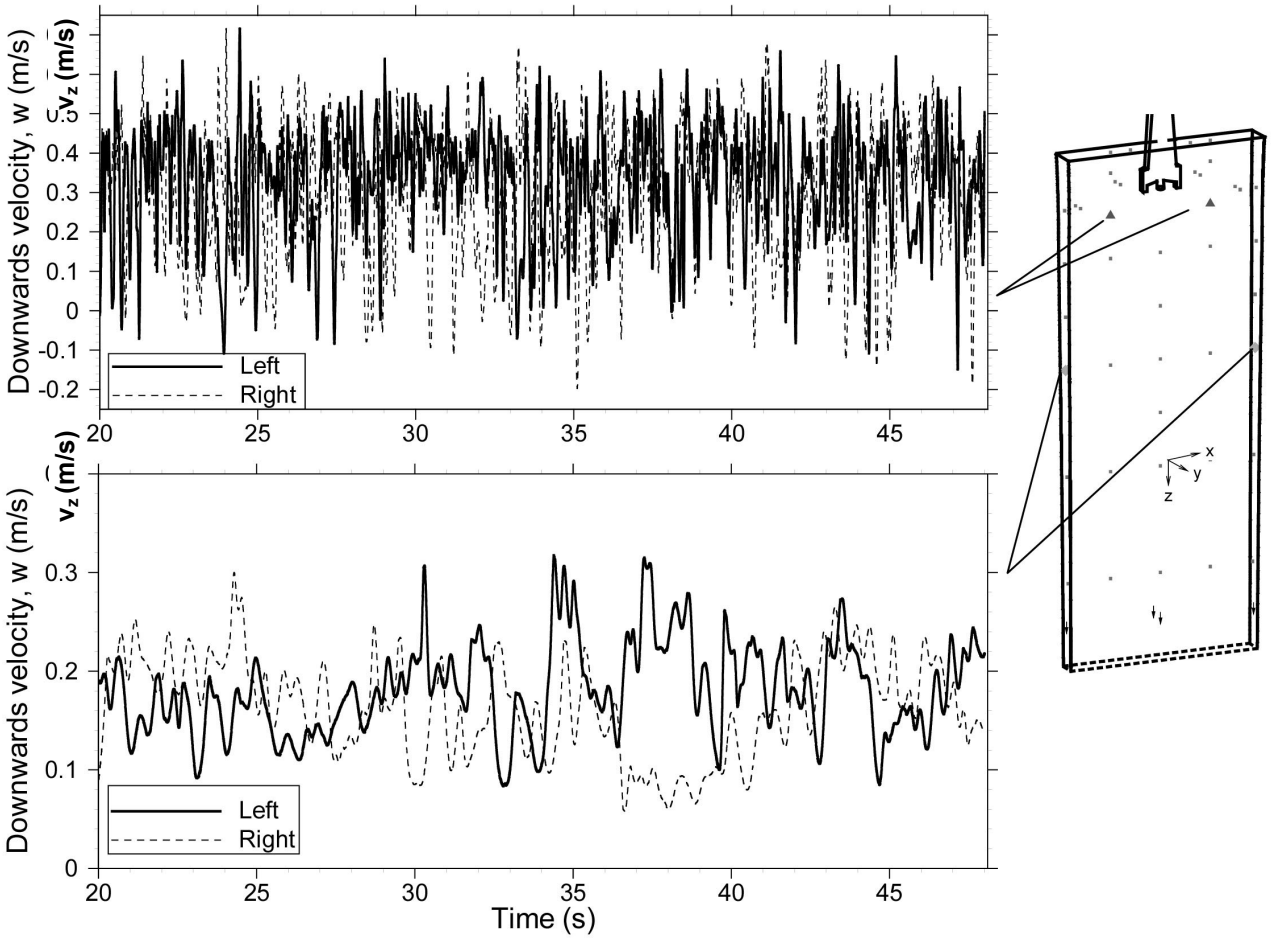


**Figure 27. Time variations of downward velocity at two pairs of symmetrical points showing low frequency asymmetries in the lower recirculation zone (*Case 2-S*).**

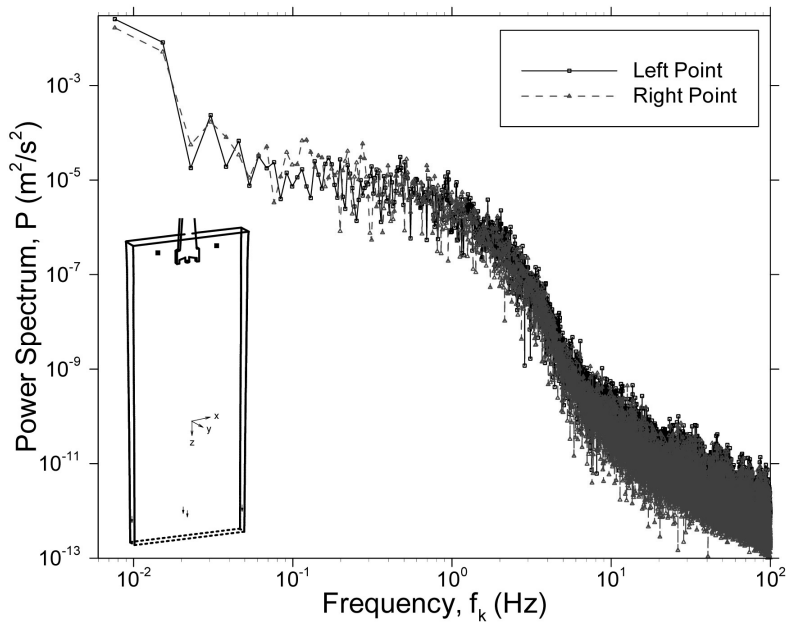


**Figure 28. Power spectrum of $v_x$ at two points in the upper mold, obtained from simulation data (*Case 2-S*).**

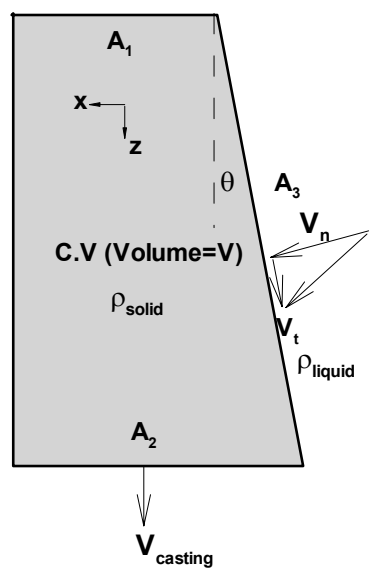


**Figure A-1. The control volume for calculating boundary velocities at the shell front.**

**Table I. Properties and conditions of the simulations.**

| Parameter/Property | *Case 1* | *Case 2-W* | *Case 2-S* |
|---|---|---|---|
| Mold Width (mm) | 1830 | 984 | 984 |
| Mold Thickness (mm) | 238 | 132 | 132 |
| Water Model Length (mm) | 2152 | 2600 | - |
| Mold Length (mm) | - | - | 1200 |
| Domain Width (mm) | 238 | 984 | 984 (top)<br>934.04 (domain bottom) |
| Domain Thickness (mm) | 238 | 132 | 132 (top)<br>79.48 (domain bottom) |
| Domain Length (mm) | 2152 | 1200 | 2400 |
| Nozzle Port Height × Thickness (mm × mm) | 51×56 (see Fig.2) | 75 × 32 (inner bore) | 75 × 32 (inner bore) |
| Bottom nozzle Port Diameter (mm) | - | 32 | 32 |
| SEN Submergence Depth (mm) | 150 | 127 | 127 |
| Casting Speed (mm/s) | 15.2 | 25.4 | 25.4 |
| Fluid Kinematic Viscosity ($m^2/s$) | $1.0 \times 10^{-6}$ | $1.0 \times 10^{-6}$ | $7.98 \times 10^{-7}$ |